Wiley
International Journal of Energy Research
Volume 2024, Article ID 8838934, 19 pages
https://doi.org/10.1155/2024/8838934

WILEY

Research Article

Transition Metal Dichalcogenides as Effective Dopants in Nanofiber-Based Triboelectric Nanogenerators

Abdulkerim Karabiber,[1] **Ömer Dirik**,[1] **Abdulkerim Okbaz**,[2,3] **Adem Yar**,[4] **Abdurrahman Özen**,[5] **and Faruk Özel**[6]

[1]*Department of Electrical and Electronics Engineering, Bingol University, Bingol 12000, Türkiye*
[2]*Department of Mechanical Engineering, Dogus University, Istanbul 34775, Türkiye*
[3]*School of Materials Science and Engineering, Georgia Institute of Technology, Atlanta 30332, GA, USA*
[4]*Department of Mechanical Engineering, Bingol University, Bingol 12000, Türkiye*
[5]*Department of Mechanical Engineering, Suleyman Demirel University, Isparta 32260, Türkiye*
[6]*Department of Metallurgical and Materials Engineering, Karamanoglu Mehmetbey University, Karaman 70200, Türkiye*

Correspondence should be addressed to Abdulkerim Okbaz; aokbaz@dogus.edu.tr

Received 19 September 2023; Revised 4 January 2024; Accepted 31 July 2024

Academic Editor: Soumyendu Roy

Triboelectric nanogenerators (TENGs) are advanced energy harvesters that convert mechanical energy in diverse environments into electrical energy via static electrification and electrostatic induction. However, their performance needs to be improved to expand their area of use and become more practical. In this study, we introduced molybdenum disulfide (MoS_2) and tungsten disulfide (WS_2) as separate additives into polyacrylonitrile (PAN) to produce composite nanofibers via electrospinning, aiming to increase the electrical output of the TENGs. This method increased contact area by narrowing the nanofiber diameters, which is a key factor in enhancing the triboelectric effect. The incorporation of MoS_2 or WS_2, characterized by high specific surface area, interface polarization, quantum confinement effects, and strong electron acceptance and trapping capabilities, led to a significant increase in the dielectric constant and overall electrical performance of the TENGs. Experimental evaluations, connecting the TENGs to circuits with various resistive loads, determined optimal performance at a load resistance of 4.7 MΩ. In particular, the 5 wt% WS_2@PAN & polyvinylbutral (PVB) and 5 wt% MoS_2@PAN & PVB TENGs exhibited a remarkable peak power output of 40.5 mW, corresponding to a power density of 25.3 W/m^2 and provided open circuit voltage of 1,026 V. The integration of 5 wt% MoS_2 or 5 wt% WS_2 led to more than a twofold increase in electrical power density compared to pristine PAN. These outcomes demonstrate the significant impact of transition metal dichalcogenides in enhancing the energy conversion efficiency of contact–separation mode TENGs, thereby contributing to the advancement of energy harvesting technology.

1. Introduction

Triboelectric nanogenerators (TENGs) are cutting-edge devices that generate electric power via contact electrification and electrostatic induction. TENGs efficiently convert mechanical motion into electrical energy across various applications. They are particularly effective at large-scale energy harvesting, utilizing sources such as wind [1, 2, 3, 4], ocean waves [5, 6, 7], and water currents [8]. On a smaller scale, TENGs efficiently generate microelectricity from biomechanical activities [9, 10, 11, 12, 13]. The expansion of the internet of things (IoT) has led to the global deployment of trillions of sensors [14]. Providing power to these sensors poses a significant challenge for traditional and centralized power systems. TENGs emerge as an ideal solution, offering a decentralized and efficient means to meet the electrical demands of these widespread sensors [15, 16]. Moreover, they can function as self-powered sensors, generating electrical signals independently without the need for an external power supply [17, 18, 19].

TENGs are classified into four main configurations based on their structural shape and triboelectrification mechanism: vertical contact separation mode [20, 21, 22, 23, 24, 25, 26, 27], the lateral sliding mode [28], the single electrode mode [29], and the free-standing triboelectric layer mode [30]. This versatility allows

TENGs to utilize a wide array of energy sources. Recent research indicates that biomechanical energy [31, 32, 33, 34, 35], vibrational movements [36, 37, 38, 39, 40], wave energy [41, 42, 43, 44, 45, 46, 47], and wind energy [48, 49, 50] are efficiently convertible into electrical energy through the application of TENG technology. Additionally, the integration of TENGs in wearable technology exhibits considerable potential. Flexible TENGs, when affixed to different parts of the human body, including the feet [51, 52, 53], wrists [32, 54, 55, 56], elbows [57, 58, 59], and fingers [55, 60, 61, 62], hold the potential to energize wearable electronic devices. These applications offer new opportunities for energy harvesting in daily activities.

Enhancing TENGs has been a focal point of recent research, aiming to increase their electrical performance. This involves optimizing energy harvesting efficiency from various sources, suited to specific operating modes. An essential approach in this process involves improving the properties of the materials, which is widely recognized as a highly effective way to enhance the performance of TENGs. Four primary methodologies have been identified for material enhancement: physical, chemical, biological, and hybrid modifications [63]. Physical modifications are further divided into nonadditive and additive categories. Nonadditive physical modification focuses on altering the contact surface's shape to expand the effective contact area [64, 65, 66, 67, 68, 69]. This alteration aims to increase the surface charge density by boosting the number of atoms involved in charge transfer. Additive physical modification, in contrast, involves incorporating different nanomaterials into the contact layer. This inclusion aims to enhance the surface charge density and induced charge density, as well as to minimize the loss of surface charge [70, 71, 72, 73, 74]. Chemical modification alters the chemical structure of the contact surface to improve its electron donation or acceptance properties [75, 76]. This alteration enhances contact electrification and increases surface charge density. Biological modification, another crucial approach, utilizes biotechnology and biomaterials known for their strong electron-donating capabilities. This capability is largely attributed to functional groups rich in nitrogen and oxygen [63, 77]. Hybrid modification, as the name suggests, combines multiple approaches (physical, chemical, or biological) to capitalize on the strengths of each. This comprehensive strategy seeks to generate a combined effect, greatly improving the overall efficiency of TENGs [63, 78, 79].

The investigation of two-dimensional (2D) layered transition metal dichalcogenides, specifically molybdenum disulfide (MoS_2) and tungsten disulfide (WS_2) compounds, has emerged as a central focus in the electronics sector, attracting considerable attention because of their distinctive characteristics [80, 81, 82]. These compounds are characterized by a wide band gap, controllable dielectric constants under electric fields, and a semiconducting nature. Their high specific surface areas, interface polarization characteristics, and exceptional electron-accepting–trapping properties position them as pivotal materials in the development of TENGs. MoS_2 has shown particular promise in TENG applications. Wu et al. [73] demonstrated this by integrating a monolayer of MoS_2 into a Kapton friction layer, achieving a 120% increase in peak power density. Further, the incorporation of MoS_2 flakes into ferroelectric materials like nylon-11 and PVDF-TrFE notably enhanced TENG performance [83]. Additionally, modifying the surface morphology of MoS_2, such as the laser-based crumpled MoS_2 surface technique developed by Park et al. [84], proved to be effective in enhancing the functional characteristics of these materials. This crumpling approach not only altered the work function but also increased the surface roughness of MoS_2, resulting in a 40% increase in power output compared to TENGs with flat MoS_2 surfaces. Karmakar et al. [85] explored the potential of flexible paper-based TENGs utilizing 2, 5, and 9-layered MoS_2 nanosheets, discovering that the maximum electrical performance was achieved with 2-layered MoS_2. In a different approach, Gallardo-Vega et al. [86] coated stainless steel with MoS_2, creating a triboelectric energy harvester for potential smart healthcare devices. Shrestha et al. [87] developed a contactless TENG, leveraging the high electron acceptability of Siloxene/Ecoflex layers to retain negative charges for extended periods, thus enhancing the TENG's sensing capabilities. MoS_2's properties also contribute to reducing mechanical wear in wind harvesting TENGs, as demonstrated by Zhao et al. [88]. They found that incorporating MoS_2 nanosheets into PVC not only enhanced the TENG's electrical performance but also extended its lifespan due to MoS_2's electron-accepting and lubricating properties. Kim et al. [89] constructed TENGs using large-sized monolayer MoS_2, comparing ohmic, Schottky, and p–n junction contacts, with the latter two showing higher output powers. Hedau et al. [90] demonstrated that embedding MoS_2 into PVDF nanocomposite films significantly enhanced TENG performance. They achieved this improvement by optimizing MoS_2 concentration and applying postannealing techniques, which resulted in increased open-circuit voltage and short-circuit current of the TENGs. WS_2, like MoS_2, is also a promising material for TENG enhancement due to its unique electrical properties, flexibility, and ultrathin nature. Kim et al. [91] introduced a novel defect engineering method for WS_2, conjugating it with thiolated ligands, which resulted in a tenfold increase in TENG performance. A self-powered Au–WS_2-based STENG for photodetection, a WS_2 nanosheet-based STENG for power generation and motion sensing, and an Au-augmented WS_2 TENG as a self-powered temperature sensor were developed by Chekke et al. [92, 93, 94]. The investigations demonstrate the adaptability of WS_2 in improving the performance of TENGs in several applications, including wearable sensors and energy-harvesting devices.

In this research, the incorporation of MoS_2 and WS_2 compounds into polyacrylonitrile (PAN) matrix notably enhanced the electrical performance of the TENGs. The study meticulously investigated the impact of these compounds, added at various concentrations, on the output voltages, current, and electric power of the TENGs. Electrospinning is a pivotal technique in nanotechnology, renowned for its versatility in creating nanofibers with precise structural control, crucial for TENGs. This method meticulously manipulates parameters like solution concentration and electrical field, influencing nanofiber diameter and thus impacting the triboelectric effect and TENG performance [95]. The resulting high surface-to-volume ratio of the

nanofibers enhances TENGs' electrical output. Furthermore, electrospinning's ability to integrate various polymeric solutions [96] allows for tailored nanofiber customization for specific applications, extending its utility across energy, medical, and environmental sectors, thereby playing a crucial role in advancing TENG technology [97, 98, 99, 100]. A critical innovation in this research was the development of a nanofiber structure through electrospinning, utilizing a nanocomposite material formed by integrating MoS_2 or WS_2 into PAN. This approach was strategically aimed at augmenting the specific surface area, electron-gaining–trapping ability, and dielectric constant of the resultant dielectric polymer–dichalcogenide composite. Key observations from the study included: first, the addition of MoS_2 or WS_2 effectively reduced the diameters of the nanofibers, thereby expanding the contact surface area available for triboelectrification; and second, the addition of MoS_2 and WS_2 increased the dielectric constant. This increase in contact area and dielectric constant played a significant role in enhancing the performance of the TENGs. Remarkably, the addition of these additives at a 5 wt% yielded the most significant performance improvement. At this concentration, the power density of the TENGs increased significantly, reaching more than double the original value. The study's findings further revealed that TENGs comprising 5 wt% MoS_2@PAN nanofibers and 5 wt% WS_2@PAN nanofibers achieved an output power density of ~25.3 W/m^2. This significant increase in power density illustrates the effectiveness of MoS_2 and WS_2 in enhancing the electrical output of TENGs when incorporated into nanofiber structures within PAN matrix. This study specifically highlights the innovative integration of MoS_2 and WS_2 into nanofibers produced through electrospinning, representing a significant advancement in TENG technology. By utilizing the unique properties of transition metal dichalcogenides in conjunction with the high surface area-to-volume ratio of electrospun fibers, this approach markedly enhanced the efficiency and flexibility of TENGs. This focused integration of MoS_2 and WS_2 into the electrospun nanofibers fills important gaps in the research and guides the development of more efficient energy harvesting systems.

2. Materials and Methods

2.1. Materials. MoS_2 (100 nm) nanopowder and WS_2 (35–75 nm) nanopowder were purchased from Nanografi. Notably, both MoS_2 and WS_2 used in this research are nanoscale particles belonging to the hexagonal crystal system's P63/mmc space group PVB and PAN ($M_w = 150{,}000$) were obtained from Sigma Aldrich. Dimethylformamide (DMF) was provided by Merck. Ethanol (C2H5OH, 99.9%) was obtained from Isolab. In this study, PAN and PVB were chosen as negative and positive materials, respectively, for their distinct electron gaining tendency properties crucial in TENGs. PAN, characterized by its nitrile groups, displays a strong electron-accepting nature due to the high electronegativity of nitrogen in the triple bond, making it an ideal tribonegative material [101] for TENGs. In contrast, PVB, with its aliphatic chains and hydroxyl groups, exhibits a tendency of losing electrons. This property categorizes PVB as a tribopositive material [102] in TENG applications.

2.2. Electrospinning Process. The electrospinning process was conducted using a direct current (DC) power supply. In this process, the positive and negative dielectric layers of the TENG system were fabricated separately. To prepare the negative layers, five solutions were prepared individually. In each container, 500 mg of PAN was dissolved in 5 ml of DMF. These solutions were then mixed using a stirrer to achieve a homogeneous mixture over 1 hr. Subsequently, varying weights of MoS_2 (1, 3, 5, and 10 wt%) were added to each solution. The mixtures were stirred continuously for 16 hr to ensure homogeneity. For the fabrication of the positive layers, a similar approach was followed. Five separate solutions were prepared, each containing 500 mg of PVB dissolved in 5 ml of ethanol. These solutions were then loaded into syringes equipped with 21-gauge needle tips, each designated for the electrospinning process. Before electrospinning, the distance between the needle tip and the aluminum (Al) foil-covered collector was set at 15 cm. The voltage and flow rates were adjusted to 20 kV and 2 ml/hr, respectively. Under these conditions, nanofibers were collected on the surface of the collector. A similar production process was applied to create the WS_2-doped dielectric layer.

2.3. Fabrication of the TENGs. The spring-supported vertical contact–separation mode TENG was constructed using plexiglass for the upper and lower backplates, dielectric materials, and Al electrodes. The movement of the plates was guided by pins and springs mounted on all four sides. As electrodes, Al foils were attached to the inner surfaces of these plates. A hole was drilled in the center of each 100 mm × 100 mm × 5 mm plexiglass pieces, allowing a cable to pass through and contact the Al electrodes. To prevent any interference from the cables during the movement of the plexiglass, a second hole, perpendicular to the first, was also drilled, and the conductive cables were inserted through this hole. During the experiments, a force of ~20 N was applied to the upper plate. This action resulted in a counteracting force from four steel springs, estimated at 10 N when fully compressed, thereby applying an effective net force of ~10 N on the test materials. To ensure unimpeded contact and avoid any mechanical issues, the dielectric materials were precisely fabricated to dimensions of 40 mm × 40 mm. The mechanical actuation, simulating biomechanical energy harvesting, was consistently regulated at a frequency of 2 Hz. A distinct TENG mechanism was carefully designed and used for each experiment.

2.4. Instrumentation and Experiments. To derive X-ray diffraction (XRD) patterns in a powdered form, a Bruker Advance D8 XRD apparatus featuring a copper α-source with a wavelength of 1.5406 Å was employed. For scanning electron microscopy (SEM) analysis, a Hitachi SU5000 scanning electron microscope was utilized. Voltage measurements within the circuit were conducted using a Rigol DS 4014 oscilloscope, featuring an input resistance of 10 MΩ, from which the electrical outputs were subsequently deduced. To

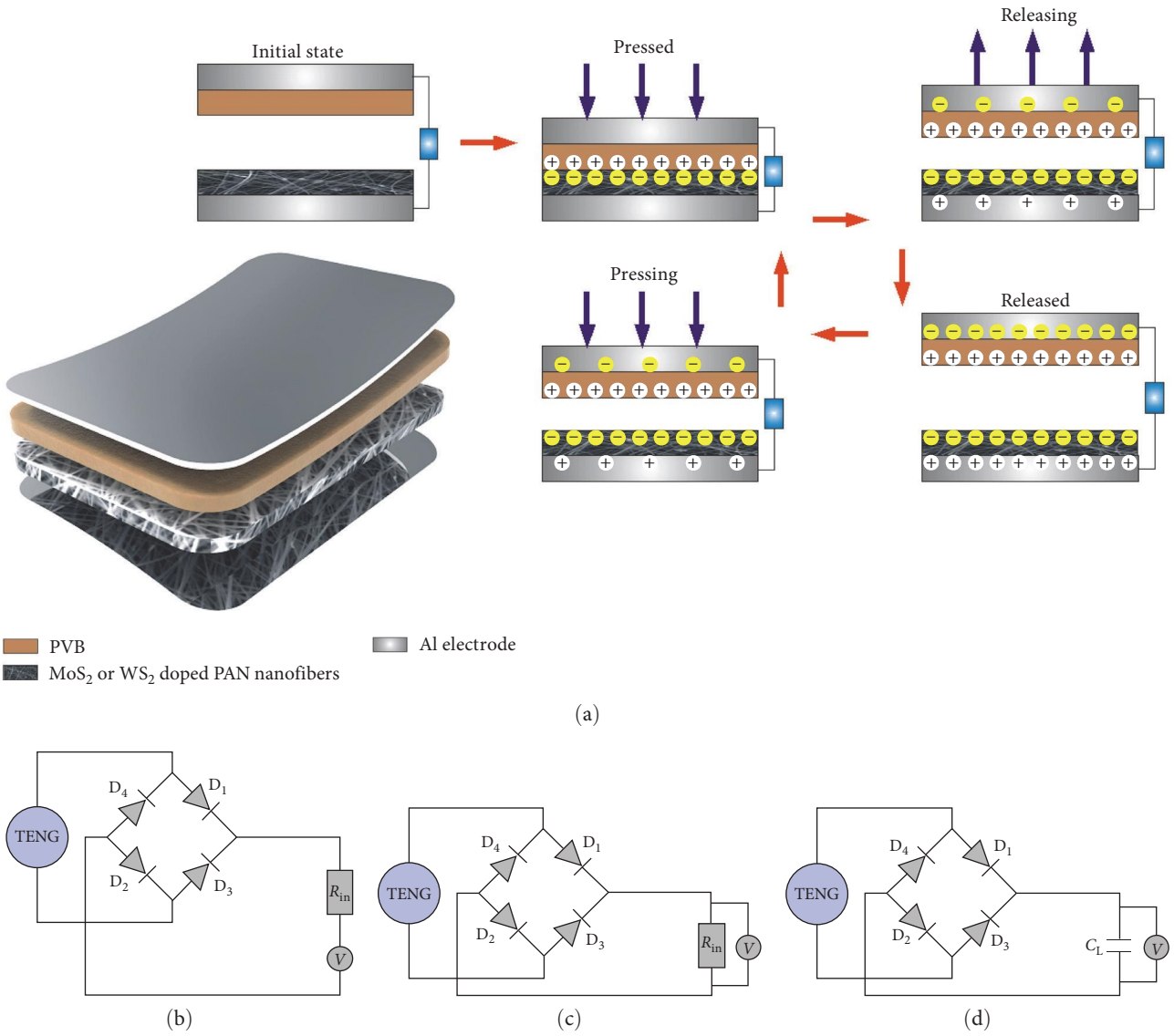

FIGURE 1: Contact–separation mode TENG overview. (a) Operational stages and structure detailing contact–separation dynamics. (b) Serial connection measurement circuit for output voltage. (c) Parallel connection measurement circuit for output voltage. (d) Voltage measurement circuit across the capacitor.

determine the dielectric constants and dielectric losses, the GW Instek LCR-6200 was utilized, facilitating precise electrical characterization.

The dielectric layers underwent manual compression and decompression, simulating biomechanical energy harvesting at a frequency of 2 Hz with an applied force of 20 N, selected to closely resemble the rhythm and force of human movement. The preference for this frequency stems from the proven efficacy of TENGs at lower frequencies compared to traditional electromagnetic generators [103]. To facilitate the conversion of AC output from the TENG to DC output, a bridge diode was integrated into the circuit, ensuring the representation of solely positive voltage and current values in our results (Figures 1(b), 1(c), and 1(d)).

The configuration for connecting the measurement apparatus to the TENG circuit—serial or parallel—was determined by the resistance values of the connected load resistors. Due to the high resistance of these resistors, we were unable to directly measure the voltage across them because of the internal resistance of the measurement device. Consequently, for circuits with high-resistance loads, the measurement device was incorporated in series to deduce the total voltage, while for low-resistance loads, a parallel connection was established. The electrical power output was quantified using the measured voltage between the metal electrodes (V) and the calculated equivalent resistance (R_{eq}), as shown in the following equation:

$$P = \frac{V^2}{R_{eq}}. \tag{1}$$

The equivalent resistance for serial connection (Figure 1(b)) was calculated using the equation below, accounting for the measurement instrument's internal resistance.

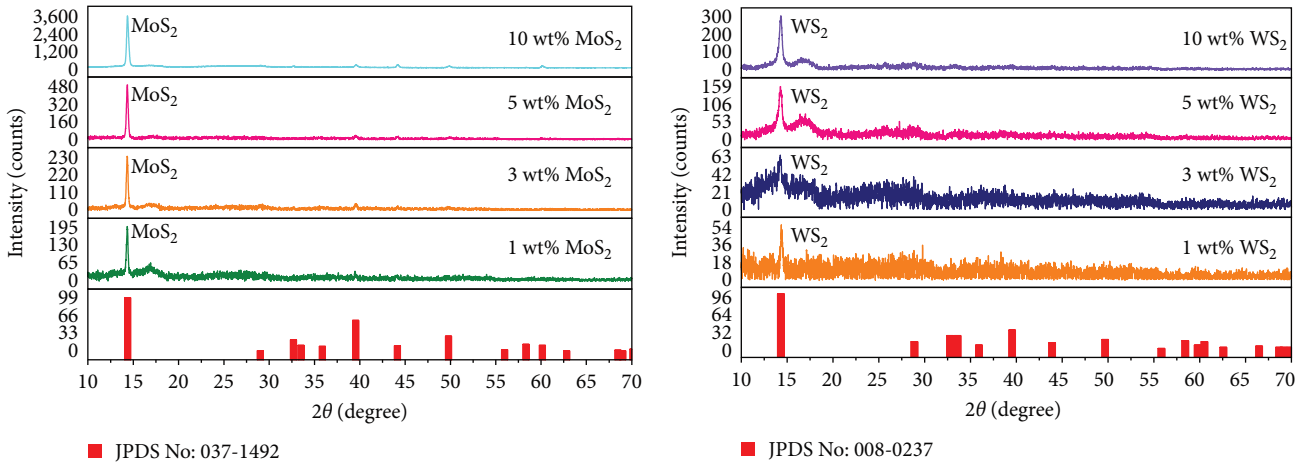

(a) (b)

FIGURE 2: XRD results of (a) MoS_2 and (b) WS_2-doped PAN nanofibers.

$$R_{eq} = R_{in} + R_L. \tag{2}$$

The equivalent resistance was determined for a parallel connection (Figure 1(c)) using the equation given:

$$R_{eq} = \frac{R_L R_{in}}{R_L + R_{in}}. \tag{3}$$

R_L represents the resistance values of connected resistors. In a serial connection, determining the voltage between the electrodes necessitates calculating the voltage difference in the load resistors. This calculation was performed using the following method:

$$V = V_m + IR_L. \tag{4}$$

In this instance, the current was determined by the following relationship:

$$I = \frac{V_m}{R_{in}}. \tag{5}$$

To evaluate the charging capabilities of the TENGs, capacitors were connected to the circuit, with their capacitances spanning from 0.022 to 1 μF (Figure 1(d)). The charge stored in each capacitor was determined by multiplying its capacitance by the voltage across it, as specified by the equation:

$$Q_c = C_L V_c. \tag{6}$$

Here, V_c represents the voltage measured across the capacitor. Subsequently, the energy storage capacity of the capacitor was calculated using the expression:

$$E_c = \frac{1}{2} C_L V_c^2. \tag{7}$$

3. Result and Discussion

3.1. Material Characteristics. The phase properties and crystal structures of MoS_2 and WS_2 doped nanofibers were investigated using XRD measurements. The results are depicted in Figure 2. In the case of the MoS_2-doped nanofibers, four primary diffraction peaks were identified. The most pronounced peak, corresponding to the (002) plane of the hexagonal structure, was observed at around $2\theta = 14.3°$. Additional significant peaks, associated with the (103), (006), and (105) planes, were noted at $2\theta = 39.5°$, 44.1°, and 49.7°, respectively (JCPDS card no. 037-1492). It was observed that all diffraction peaks were intense and well-defined. Moreover, an increase in the intensity of these peaks was correlated with the increment in MoS_2 content. For the WS_2-doped nanofibers, diffraction peaks similar to those in the MoS_2-doped nanofibers were detected. The highest peak among these was found at ~$2\theta = 14.3°$, with another significant peak occurring at around $2\theta = 39.5°$. These peaks were identified as corresponding to the (002) and (103) planes (JCPDS no. 008-0237), confirming the crystallographic structure of the WS_2-doped nanofibers.

Figures 3(a), 3(b), 3(c), 3(d), 3(e), 3(f), 3(g), and 3(h) and 4(a), 4(b), 4(c), 4(d), 4(e), 4(f), 4(g), and 4(h) show the SEM images of nanofibers doped with varying amounts of MoS_2 and WS_2 captured at different magnifications, respectively. It was observed in these images that all fibers displayed a homogeneous distribution and a smooth surface. Notably, no beaded structures were detected on the fiber surfaces. However, as the concentration of MoS_2 and WS_2 increased, agglomeration issues were observed. This agglomeration on the nanofibers was identified as a crucial factor affecting the TENG's output performance. A homogeneous dispersion of these substances was maintained up to a doping concentration of 5 wt%, beyond which agglomeration began to occur. This observation was corroborated by the electrical measurement results, which indicated that the maximum output performance was achieved at a 5 wt% doping concentration.

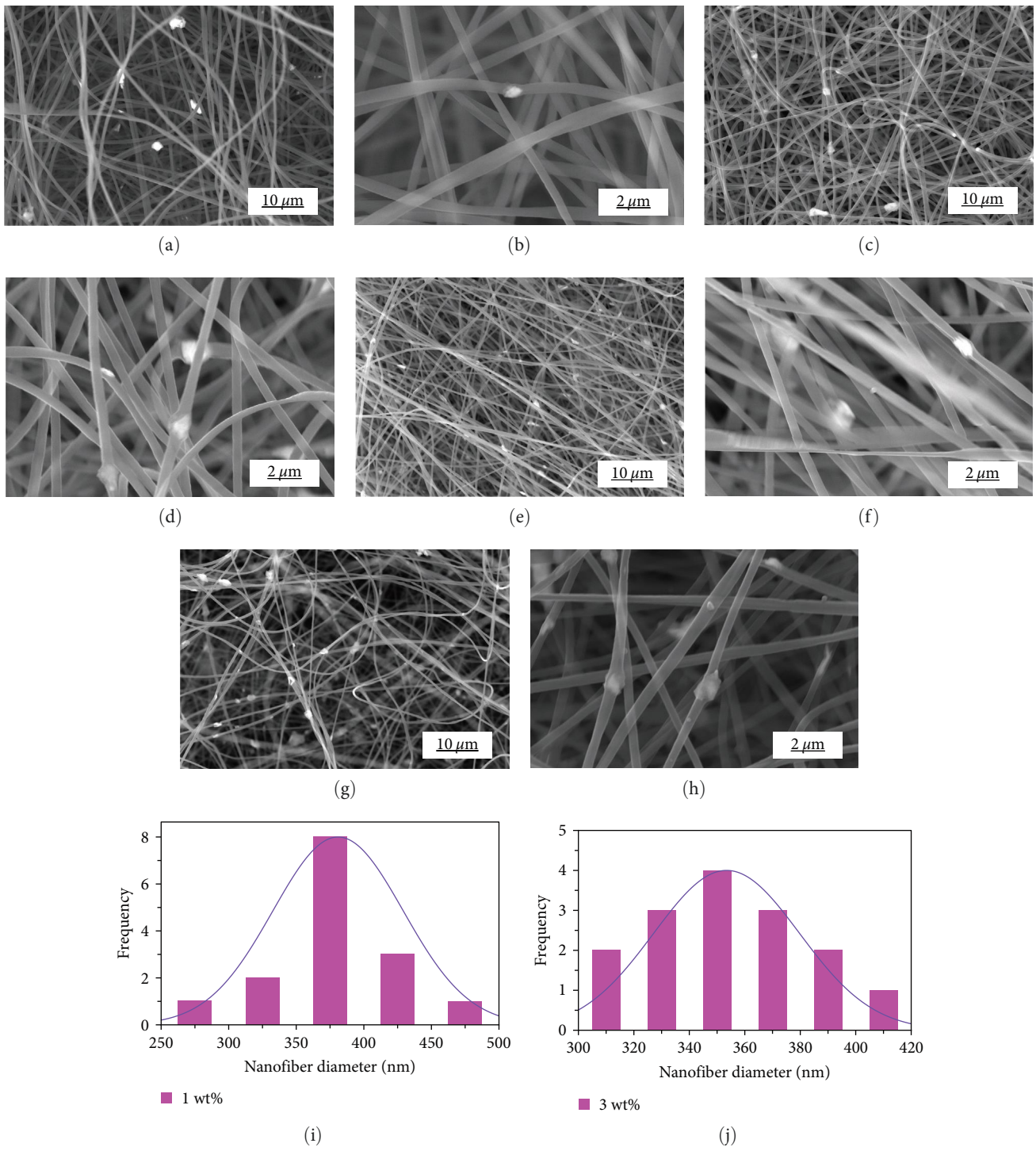

Figure 3: Continued.

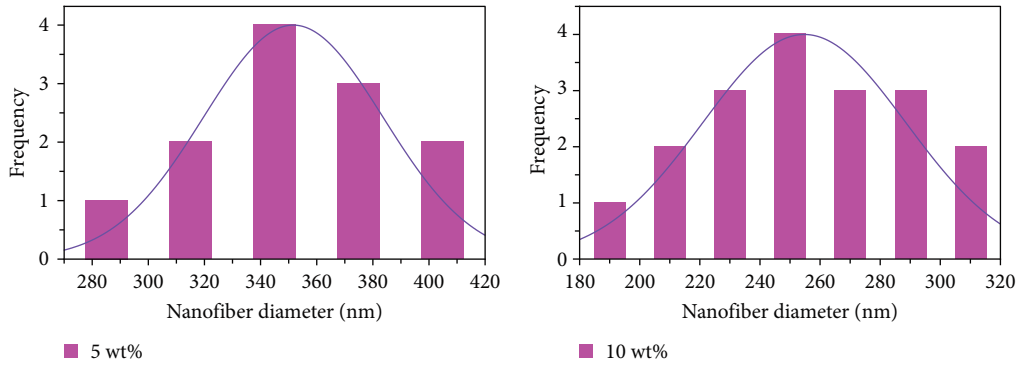

(k) (l)

FIGURE 3: SEM images of (a and b) 1 wt%, (c and d) 3 wt%, (e and f) 5 wt%, and (g and h) 10 wt% MoS_2-doped PAN nanofibers, respectively. (i–l) Size distribution graphs of MoS_2-doped PAN nanofibers with different ratios.

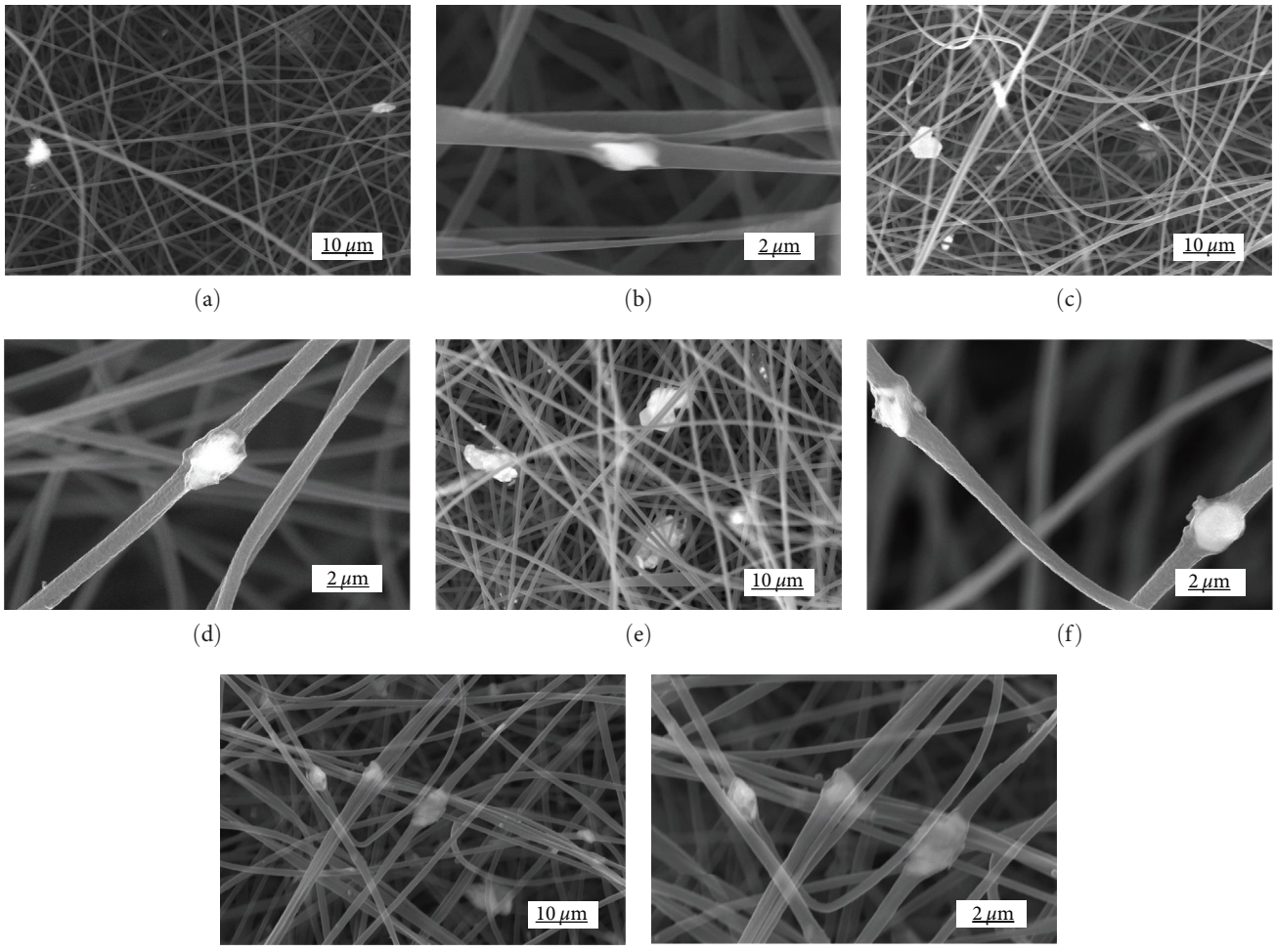

(a) (b) (c)

(d) (e) (f)

(g) (h)

FIGURE 4: Continued.

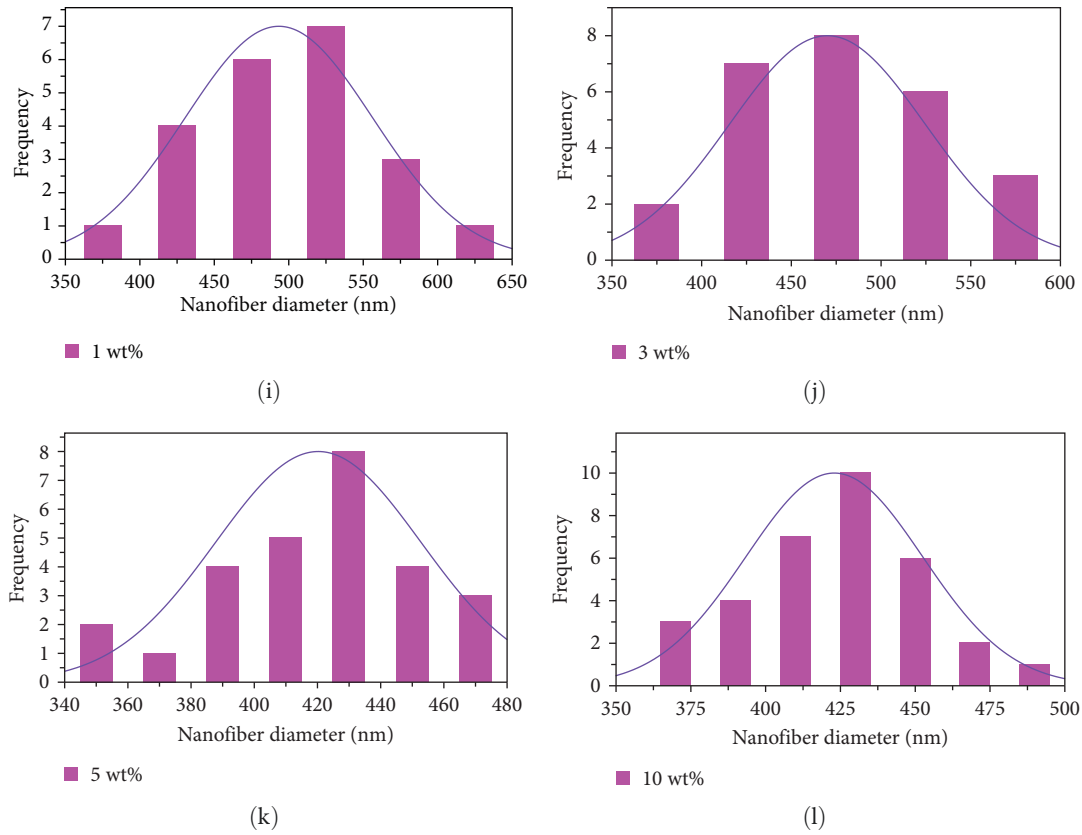

FIGURE 4: SEM images of (a and b) 1 wt%, (c and d) 3 wt%, (e and f) 5 wt%, and (g and h) 10 wt% WS_2-doped PAN nanofibers, respectively. (i–l) Size distribution graphs of WS_2-doped PAN nanofibers with different ratios.

Beyond this rate, a decrease in TENG output performance was noted. Figures 3(i), 3(j), 3(k), and 3(l), and 4(i), 4(j), 4(k), and 4(l) illustrate the size distribution of the synthesized nanofibers. Analysis revealed that the mean diameters for MoS_2-doped nanofibers were 375 ± 25, 350 ± 30, 345 ± 25, and 250 ± 40 nm, while WS_2-doped nanofibers exhibited average diameters of 500 ± 50, 475 ± 50, 430 ± 30, and 425 ± 25 nm, at doping concentrations of 1, 3, 5, and 10 wt%, respectively.

3.2. Electrical Outputs of the TENGs. Figure 1(a) shows the operation of a TENG in vertical contact–separation mode, detailing the sequence of electrical power generation. Initially, the triboelectric materials are electrically neutral, carrying no net positive or negative charges. Manual actuation forces the tribopositive material to move toward the tribonegative counterpart. Triboelectric charges of opposite polarities accumulate on the surfaces of the materials during contact. Upon releasing the applied force, the inherent tension in the TENG's springs causes the materials to separate from each other. This separation phase leads to electrostatic induction due to the presence of opposite charges over the surfaces of triboelectric materials, thereby creating a potential difference between the electrodes. When the circuit is closed, this potential difference drives an electrical current as charges move through the conductors. The current flows until a state of charge equilibrium is reached, nullifying the potential difference via charge redistribution. Subsequent reverse movement disrupts this equilibrium, triggering a flow of electrons in the opposite direction and giving rise to a renewed generation of electric current. When the triboelectric materials come into full contact, the equilibrium of electric charges is restored, which stops the flow of electric current. Alternating current (AC) will continue to be generated in this manner as a consequence of movements that are repeated at regular intervals. To power electronic devices, the AC generated by the TENG is converted to DC using rectification circuits, including bridge diodes and rectifiers [104].

Figure 5 illustrates the voltage (Figures 5(a) and 5(d)), the voltage across the capacitor (Figures 5(b) and 5(e)), and the peak power (Figures 5(c) and 5(f)) for WS_2 and MoS_2 additives, measured at a 10 MΩ load resistance, with a 0.022 μF capacitive load, and under varying load resistances, respectively. TENGs operating in contact–separation mode typically generate a periodically varying voltage output. Each manual actuation of the TENGs generated a dual-peak voltage pattern, with one prominent peak and one smaller peak, followed by a rapid decline, as shown in Figures 5(a) and 5(d). The periodic nature of these signals can be utilized to deduce the frequency of the force acting on the TENG layers, which was determined to be 2 Hz. The incorporation of WS_2 or MoS_2 significantly influenced the TENG output voltages. The addition of WS_2 resulted in a substantial increase in output voltage, reaching its maximum at a 5 wt% concentration. However, increasing the additive ratio to 10 wt% led to a sharp decrease in output

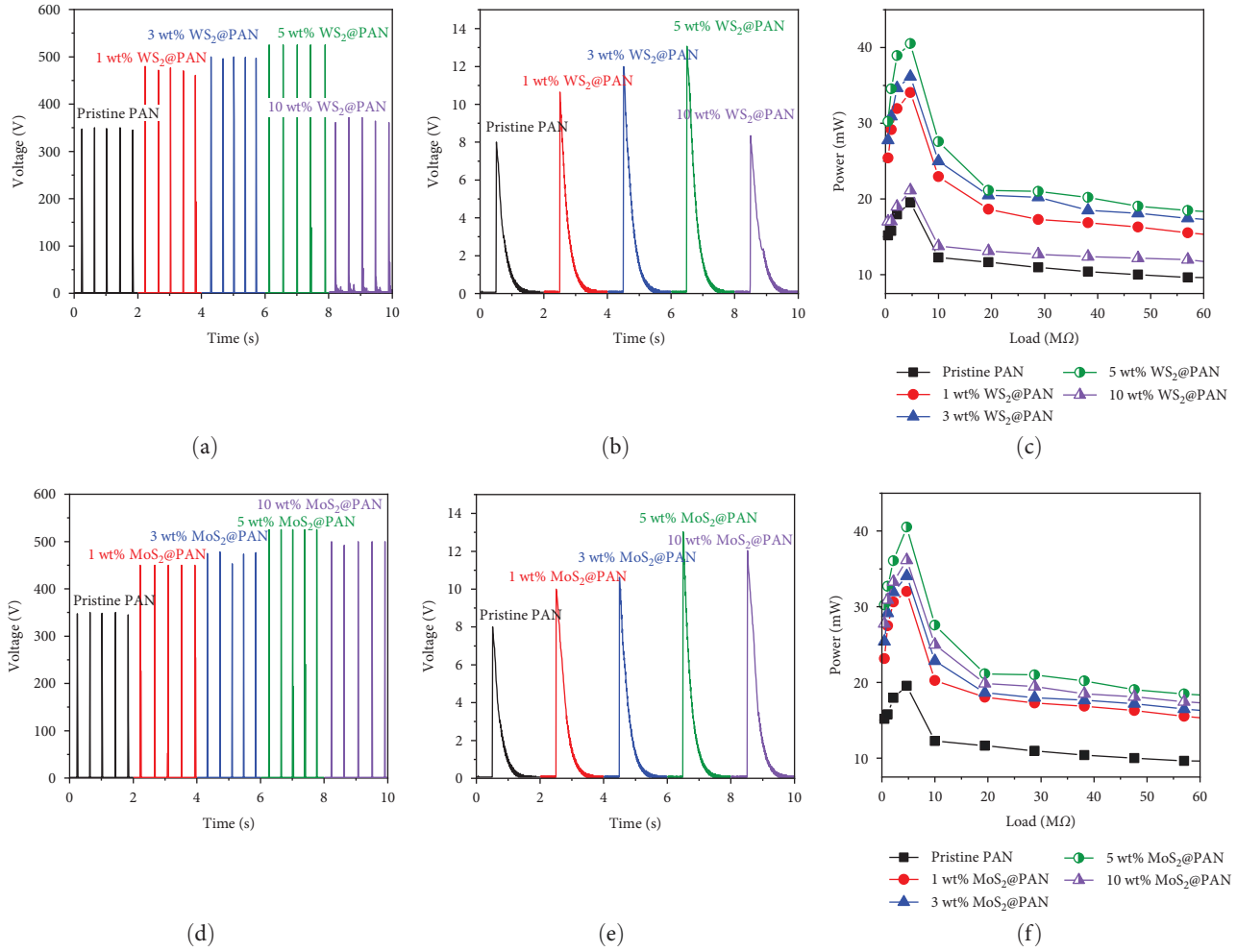

FIGURE 5: Performance characteristics of WS_2@PAN & PVB and MoS_2@PAN & PVB TENGs. (a) Output voltage at 10 MΩ for WS_2@PAN & PVB. (b) Voltage across the capacitor at 0.022 μF for WS_2@PAN & PVB. (c) Peak power curves for WS_2@PAN & PVB. (d) Output voltage at 10 MΩ for MoS_2@PAN & PVB. (e) The voltage across the capacitor at 0.022 μF for MoS_2@PAN & PVB. (f) Peak power curves for MoS_2@PAN & PVB.

voltage, approaching the levels observed in pristine PAN. Specifically, the peak output voltages at a 10 MΩ load resistance for TENGs constructed with pristine PAN and those doped with 1, 3, 5, and 10 wt% WS_2 were 350, 480, 500, 525, and 372 V, respectively. The addition of 5 wt% WS_2 proved to be the most effective, enhancing the output voltage by up to 50% compared to pure PAN. In a similar trend, MoS_2 doping at 5 wt% enhanced the peak output voltage to 525 V. However, increasing the MoS_2 concentration to 10 wt% led to a slight decrease in performance, with the output voltage dropping to 500 V. Although there was a decline, TENGs with a higher MoS_2 concentration still generated a peak voltage that was much higher than that of the undoped PAN. This highlights the positive effect of the dopants on the electrical output of the TENGs.

TENGs serve not only as generators of current and voltage signals but also as sources of electrical power, capable of directly powering systems or charging devices. Consequently, the charging feature is a significant aspect of the electrical characteristics of TENGs. To quantify the energy generated by the TENGs, a bridge diode was employed to connect them to a capacitor. Figure 5(b) presents a detailed comparison of the peak voltages across a 0.022 μF capacitor for TENGs configured with various concentrations of WS_2. The pristine PAN TENGs exhibited a peak voltage of 8 V. The integration of WS_2 as a dopant markedly improved TENG performance. Specifically, the device doped with 1 wt% WS_2 exhibited a voltage of 10.7 V, which increased to 12 V with 3 wt% doping, and further reached a peak voltage of 13.1 V at 5 wt% WS_2. However, a subsequent increase to 10 wt% WS_2 resulted in a reduced peak voltage of 8.35 V, suggesting that the optimal doping concentration for maximizing the triboelectric properties of the TENGs is 5 wt% WS_2. A capacitor, which stores electrical charges generated by the TENGs after a single mechanical agitation, was used to facilitate the determination of charge storage using Equation (6). The inclusion of WS_2 significantly altered the charge storage capabilities. The TENGs with 1, 3, 5, and 10 wt% WS_2 doping demonstrated increased charge storage capacities of 234, 264, 288, and 184 nC, respectively. This data illustrates a progressive enhancement in charge storage with the incorporation of WS_2 up to 5 wt%,

beyond which a slight reduction in stored charge occurs at 10 wt%. For comparison, the TENGs made with plain PAN stored 176 nC of charge, highlighting the significant improvements achieved with WS_2 doping. Additionally, TENGs with 5 wt% MoS_2-doped PAN achieved a higher charge transfer of 286 nC, demonstrating the effectiveness of MoS_2 in enhancing the energy-harvesting performance of the TENGs.

The electric power of a TENG varies with the resistor connected to the circuit. There is an optimal resistance at which the electric power reaches its maximum, dependent on the TENG's construction and operating conditions. Determining this optimal operating resistance requires testing under various load resistances. This was accomplished by connecting load resistors ranging from 0.5 to 57 MΩ to the circuit and recording the peak electric power outputs (Figures 5(c) and 5(f))). The comprehensive testing of the TENG models showed that the highest electric power outputs were consistently achieved at an optimal resistance of 4.7 MΩ. Using these TENGs with resistance either higher or lower than this value results in lower electric power output, clearly establishing 4.7 MΩ as the optimum resistance for these devices. For TENGs using pristine PAN, the peak power was recorded at 19.5 mW. This performance was significantly improved with WS_2 doping. TENGs with 1, 3, 5, and 10 wt% WS_2 yielded peak powers of 34.1, 36.2, 40.5, and 21.1 mW, respectively, with the 5 wt% doping level providing a substantial 2.08-fold increase in electric power compared to the pristine PAN. Similarly, MoS_2 doping also led to improved power outputs. TENGs with 1, 3, 5, and 10 wt% MoS_2 showed power outputs of 32, 34.1, 40.5, and 36.2 mW, respectively. These results highlight the significant role of both WS_2 and MoS_2 dopants in elevating the electric power generation of the TENGs. Most notably, the TENGs doped with either 5 wt% WS_2 or 5 wt% MoS_2 achieved the highest power density of 25.3 W/m^2.

Figures 6(a) and 6(d)) shows changes in TENG output voltage and current magnitudes under different load resistances. Under lower load resistances, higher currents were passed and voltage values were lower. An increase in load resistance caused the voltage to rise while significantly reducing the current due to ohmic losses. Upon reaching a certain level of load resistance, the voltage value reached a saturation point and its increase slowed. The obtained current and voltage curves align with previously published experimental and theoretical findings [105, 106]. Specifically, at a high load resistance of 57 MΩ, pristine PAN & PVB TENG reached a peak voltage of 741 V. This voltage was notably enhanced with WS_2 doping, exhibiting peak voltages of 941, 998, 1,026, and 827 V for 1, 3, 5, and 10 wt% WS_2@PAN & PVB TENGs, respectively. Similarly, adding MoS_2 to the TENGs significantly increased the output voltages to 941, 969, 1,026, and 998 V for 1, 3, 5, and 10 wt% MoS_2, respectively. Adding 5 wt% WS_2 or MoS_2 to the TENGs increased the output voltages by about 38.5%.

Figures 6(b) and 6(e) illustrates the variations in peak power for different load resistances according to the addition ratios of WS_2 and MoS_2, respectively. TENG power generation was highly dependent on the additive amount, with the highest power at all additive ratios generated at 4.7 MΩ load resistance. Power values increased up to 5 wt% with both additives, but further additions caused a decline. Performance drop was more pronounced when the WS_2 additive was increased to 10 wt%. The optimal addition rate for both WS_2 and MoS_2 was found to be 5 wt%.

The TENG power outputs previously mentioned were derived from peak voltages. However, the power generated by the periodic movement of the dielectric layers in TENGs also varies over time. Thus, assessing a TENG's capability to provide sufficient electricity for a system based solely on peak power can be challenging. Integrating a capacitor into the circuit enables the precise determination of the amount of electricity generated by a TENG over a defined period. In such cases, the electrical energy generated is utilized to charge the capacitor. An important consideration is that the amount of charge and electrical energy stored varies with different capacitive loads, similar to how electric power generated by a TENG varies with different resistive loads. Maximizing the stored charge and energy is crucial for ensuring that the powered device operates over an extended period. Additionally, the voltage across the capacitor is a critical factor since electronic devices operate within specific voltage ranges. To evaluate the TENG charging characteristics, capacitors with various capacitances, ranging from 0.1 to 1 μF, were connected to the TENG circuit and tested. The results for 5 wt% WS_2@PAN & PVB and 5 wt% MoS_2@PAN & PVB TENGs are presented in Figures 6(c) and 6(f), respectively. It was observed that as capacitance values decreased, the voltage values across the capacitor increased. Conversely, capacitors with larger capacitance values retained more charge, resulting in longer discharge times as the capacitance increased. Equation (6) facilitated the calculation of stored charge amounts. For 5 wt% WS_2@PAN & PVB TENGs, the charge stored in 0.1, 0.3, 0.5, and 1 μF capacitors w calculated to be 428, 440, 478, and 456 nC, respectively. As capacitance increased, the quantity of stored charge initially rose and then declined, with the maximum charge stored in the 0.5 μF capacitor. A similar trend was observed for 5 wt% MoS_2@PAN & PVB TENGs, where the charge amounts stored in the 0.1, 0.3, 0.5, and 1 μF capacitors were 388, 576, 584, and 546 nC, respectively.

Using Equation (7), the energy stored in the capacitors can be calculated based on the voltage across the capacitor and its capacitance. This analysis is crucial for determining the optimal capacitance value for effective energy storage. However, when comparing capacitors based on stored energy, it is evident that the capacitor storing the most energy may differ from the one storing the most charge. This is due to the energy varying proportionally to the square of the voltage, making voltage a critical parameter. For 5 wt% WS_2@PAN & PVB TENG, the energy stored in 0.1, 0.3, 0.5, and 1 μF capacitors was calculated to be 916, 322, 228, and 104 nJ, respectively. For 5 wt% MoS_2@PAN & PVB TENG, the energy stored in 0.1, 0.3, 0.5, and 1 μF capacitors was 751, 554, 341, and 149 nJ, respectively. In both cases, the 0.1 μF capacitor stored the largest amount of energy.

In the context of using TENGs as viable power sources, a crucial factor is their ability to generate enough electric power to

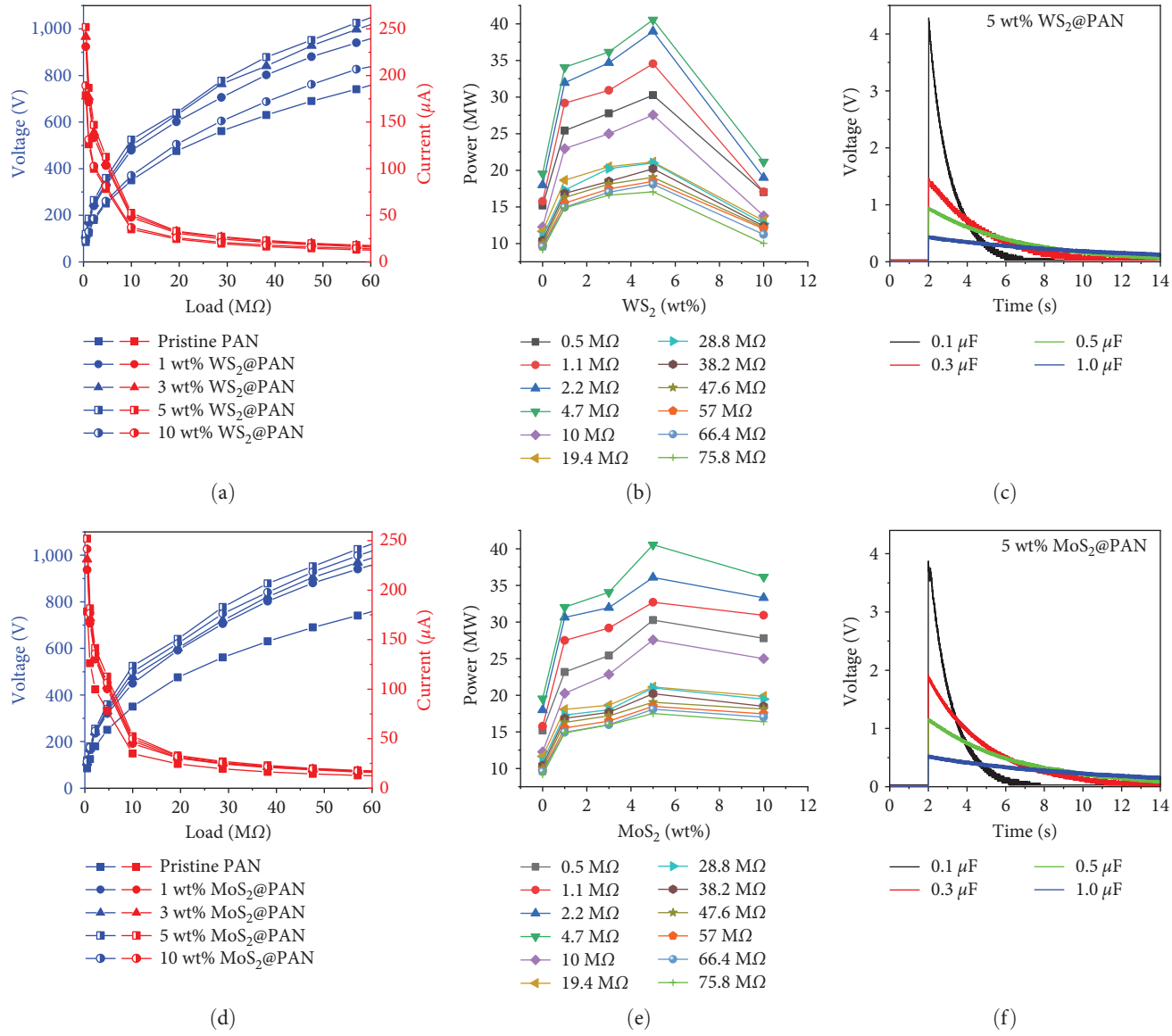

FIGURE 6: Electrical performance metrics for WS_2 and MoS_2 doped PAN and PVB TENGs. (a) Current and voltage curves for WS_2@PAN & PVB. (b) Peak power curves for WS_2@PAN & PVB. (c) The voltage across the capacitor for WS_2@PAN & PVB. (d) Current and voltage curves for MoS_2@PAN & PVB. (e) Peak power curves for MoS_2@PAN & PVB. (f) The voltage across the capacitor for MoS_2@PAN & PVB.

meet the demands of electronic devices. This study examines increasing the total electric power by connecting TENG units in parallel. This method increases the current in the circuit, thereby expanding the range of devices that TENGs can power. Experimental evidence from the parallel connection of three TENGs substantiates this approach. The output voltages at a 10 MΩ load resistance for a series of TENG configurations, specifically those incorporating 5 wt% WS_2@PAN & PVB and 5 wt% MoS_2@PAN & PVB, consistently yielded voltages ~525 V (Figures 7(a) and 7(b)). Subsequent investigations, presented in Figures 7(c) and 7(d), revealed that increasing the number of TENGs in a parallel arrangement led to a corresponding increase in the voltages measured across the 0.022 μF capacitor. This increase in voltage directly correlates with heightened electricity generation and improved energy accumulation in the capacitors. Specifically, the 5 wt% WS_2@PAN & PVB TENG exhibited capacitor voltages ranging from 14.1 to 39.9 V, depending on the number of TENGs connected in the circuit. Similarly, the voltage outputs of the 5 wt% MoS_2@PAN & PVB TENG ranged from 13.25 to 39.8 V under similar conditions. Significantly, these parallel configurations enable precise adjustment of the charging voltages to meet the individual operational requirements of various electronic devices, hence enhancing the stored energy as well. Quantitative evaluations showed that increasing the number of TENGs from one to three resulted in a significant increase in the stored electrical energy in the capacitors of the 5 wt% WS_2@PAN & PVB TENG. The stored energy rose from 2,187 to 17,512 nJ. A similar increase was observed in the 5 wt%

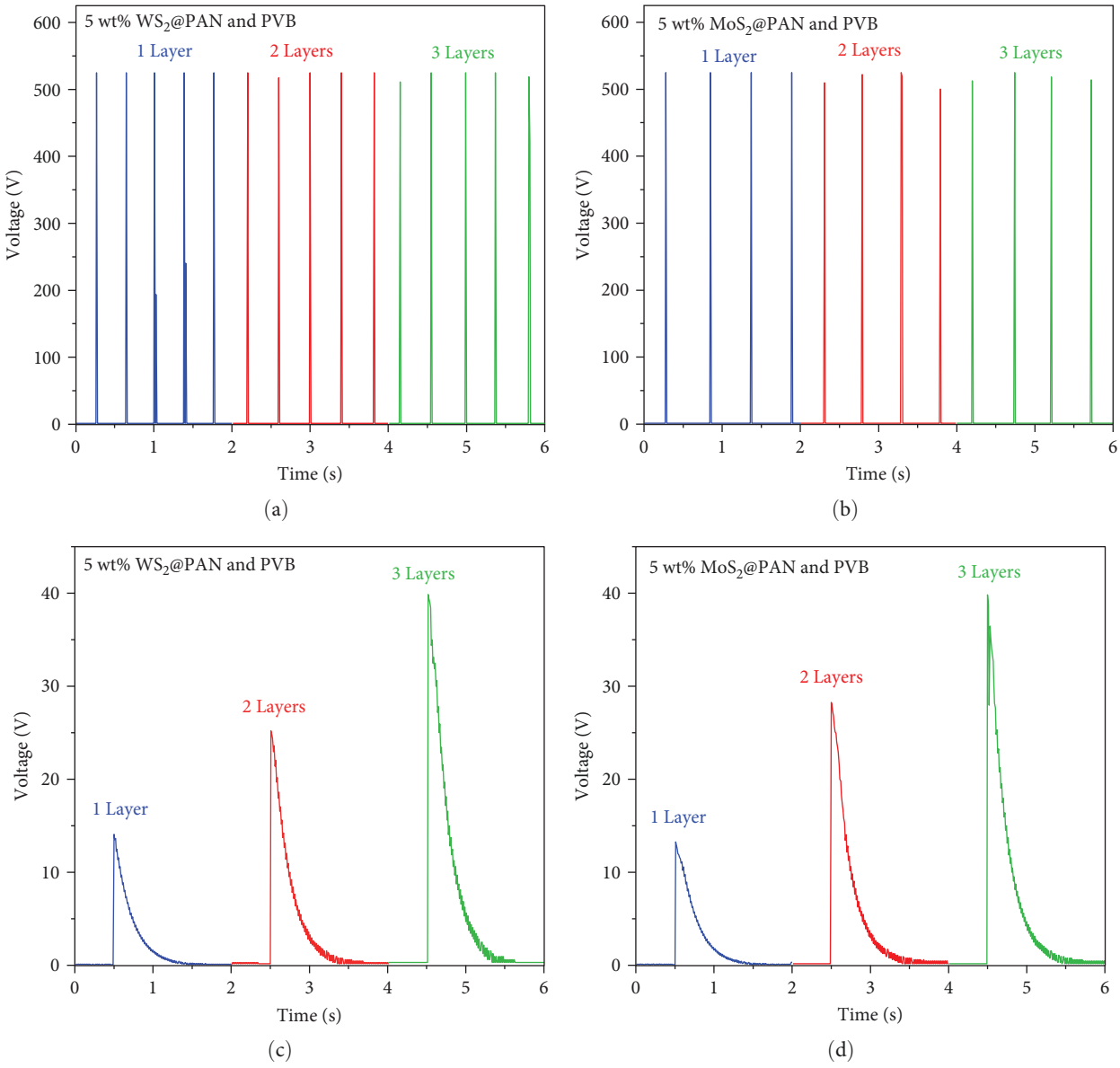

FIGURE 7: Output voltage and capacitor voltage responses in layered TENGs. (a) Output voltages under resistive load of 10 MΩ for 5 wt% WS_2@PAN & PVB TENGs. (b) Output voltages under resistive load of 10 MΩ for 5 wt% MoS_2@PAN & PVB TENGs. (c) The voltage across a 0.022 μF capacitor for 5 wt% WS_2@PAN & PVB TENGs. (d) The voltage across a 0.022 μF capacitor for 5 wt% MoS_2@PAN & PVB TENGs, providing a comparative view of the electrical performance across multiple layers.

MoS_2@PAN & PVB TENG, where the stored energy rose from 1,931 to 17,424 nJ when the number of TENGs was increased threefold.

3.3. Mechanisms of Enhancing the Electrical Output of the TENG. The inclusion of WS_2 or MoS_2 has significantly enhanced the electrical performance of the TENG. To further understand how to improve TENG performance, the *V*–*Q*–*x* relationship can be employed. The relationship between three variables, such as the voltage (*V*) between the two electrodes, the quantity of charge transferred (*Q*), and the separation distance (*x*(*t*)), is described by the *V*–*Q*–*x* relationship [105]:

$$V = -\frac{Q}{S\varepsilon_0}\left(\frac{d_1}{\varepsilon_{r1}} + \frac{d_2}{\varepsilon_{r2}} + x(t)\right) + \frac{\sigma x(t)}{\varepsilon_0}. \quad (8)$$

Here, d_1 and d_2 are the thicknesses of triboelectric materials, ε_{r1} and ε_{r2} are the dielectric constants of triboelectric materials, and ε_0 is the permittivity of the vacuum. $x(t)$ refers to the instantaneous distance between the dielectrics and *S* is the surface area of the electrodes and dielectrics. Under various load resistances, the *V*–*Q*–*x* relationship can be solved to obtain time-dependent TENG electrical outputs. In the case of an open circuit, no current flows through the circuit, implying that there is no flow of charge from one electrode to the next

($Q = 0$), and the V–Q–x relation is reduced to Equation (9) [105]:

$$V_{OC} = \frac{\sigma x(t)}{\varepsilon_0}. \tag{9}$$

In the case of a short circuit, where no resistor is connected to the circuit and the total resistance is theoretically zero, the voltage between the electrodes becomes zero. Consequently, the quantity of transferred charge is described by Equation (10) [105]:

$$Q_{SC} = \frac{S\sigma x(t)}{d_0 + x(t)}. \tag{10}$$

The current in the circuit is determined as follows [105]:

$$I_{SC} = \frac{dQ_{SC}}{dt} = \frac{S\sigma d_0}{(d_0 + x(t))^2}\frac{dx}{dt} = \frac{S\sigma d_0 v(t)}{(d_0 + x(t))^2}. \tag{11}$$

Here, d_0 is the effective dielectric thickness.

$$d_0 = \frac{d_1}{\varepsilon_{r1}} + \frac{d_2}{\varepsilon_{r2}}. \tag{12}$$

When a TENG is utilized alongside a load resistor, the voltage and current values are determined using Equations (13) and (14) [105]:

$$V = IR = R\frac{dQ}{dt}, \tag{13}$$

$$R\frac{dQ}{dt} = -\frac{Q}{S\varepsilon_0}\left(\frac{d_1}{\varepsilon_{r1}} + \frac{d_2}{\varepsilon_{r2}} + x(t)\right) + \frac{\sigma x(t)}{\varepsilon_0}. \tag{14}$$

The V–Q–x relationship outlines the influence of material characteristics, dimensions, and operational factors on the electrical outputs of TENGs. Enhancing TENG size, material dielectric constants, and surface charge densities emerges as a strategic approach to optimize electrical output performance. Considering these three distinct parameters, the underlying mechanisms for augmented TENG efficiency following the incorporation of MoS_2 or WS_2 are elucidated here. Recalling that S symbolizes the surface area of dielectric materials, it is evident that as the length and width of these materials increase, so too does S and, consequently, the size of the TENG. Expanding the dimensions of a TENG is a direct method for enhancing electric power generation without necessarily requiring changes to the surface charge density. However, increasing the effective contact area proves to be a more efficient technique, leading to an increase in surface charge density and, thus, facilitating the creation of compact, high power density TENGs. An essential strategy involves expanding the effective contact surface by increasing the material's specific surface area through nonadditive physical methods.

Contact electrification, a phenomenon involving charge transfer due to material contact, is best described by the electron cloud potential well model, as outlined in references [107, 108]. Here, electron clouds in atomic or molecular orbitals create potential wells, with loosely bound electrons in the outer shells. Electron transfer occurs when the energy barriers of potential wells are surpassed as atoms come closer, causing the potential wells to overlap and disrupting the symmetry of the potential wells. This interaction lowers energy barriers and electrons can move from higher to lower energy levels. This process requires the application of external force, particularly as atoms experience repulsive forces when they are at bond length proximity. Overcoming this repulsion force brings atoms close enough for potential well interaction and electron transfer. The applied force to the triboelectric material is, thus, a critical factor. Nonetheless, due to surface morphology, not all atoms achieve the necessary proximity for potential well overlap.

Nanofibers create a rough extended contact surface, optimizing electron transfer. Adding MoS_2 or WS_2 to the PAN matrix reduced the nanofiber diameters, increasing TENG electrical outputs by enhancing the contact area for the same material volume. However, exceeding 5 wt% addition of these materials resulted in diminished electrical performance due to several factors. An increase in surface area does not necessarily correspond to a rise in physical contact area, which depends on specific surface interactions. Engineered surface roughness, when strategically designed, typically increases the contact area [109, 110, 111, 112], thereby boosting TENG's performance. In contrast, randomly induced surface irregularities may reduce the effective contact area, potentially leading to decreased TENG performance [113, 114, 115]. This reduction is often due to air gaps formed between the mismatched indentations and protrusions on the contact surfaces of the triboelectric materials. Furthermore, the challenge of precisely evaluating the contact surface structure at the point of contact hinders the accurate determination of the effective contact area.

The tendency of the friction surface to gain or lose electrons represents another crucial factor in increasing surface charge density. The use of materials with different polarities enhances contact electrification. Additionally, the polarities of the friction surfaces of existing materials can be increased through various methods. For example, incorporating nanomaterials with a high electron-trapping capability into a tribonegative material improves the electron-accepting capacity of the friction surface [63]. It has been demonstrated that MoS_2 and WS_2 exhibit more tribonegative characteristics than PAN in the triboelectric series table [116]. The quantum confinement effect significantly impacts the tendency of materials like MoS_2 and WS_2 to gain electrons, particularly at the nanoscale. This effect arises when the dimensions of these materials are reduced to such an extent that they impede electron movement, leading to distinct energy levels [117]. The quantum confinement effect modifies the electronic properties of MoS_2 and WS_2, thereby enhancing their ability to gain electrons. This increase in the ability to gain electrons is vital for the friction surfaces of tribonegative materials, where efficient electron capture and transfer are essential for higher power generation efficiency. Therefore, integrating MoS_2 [118, 119, 120] or WS_2 [121, 122, 123] materials into

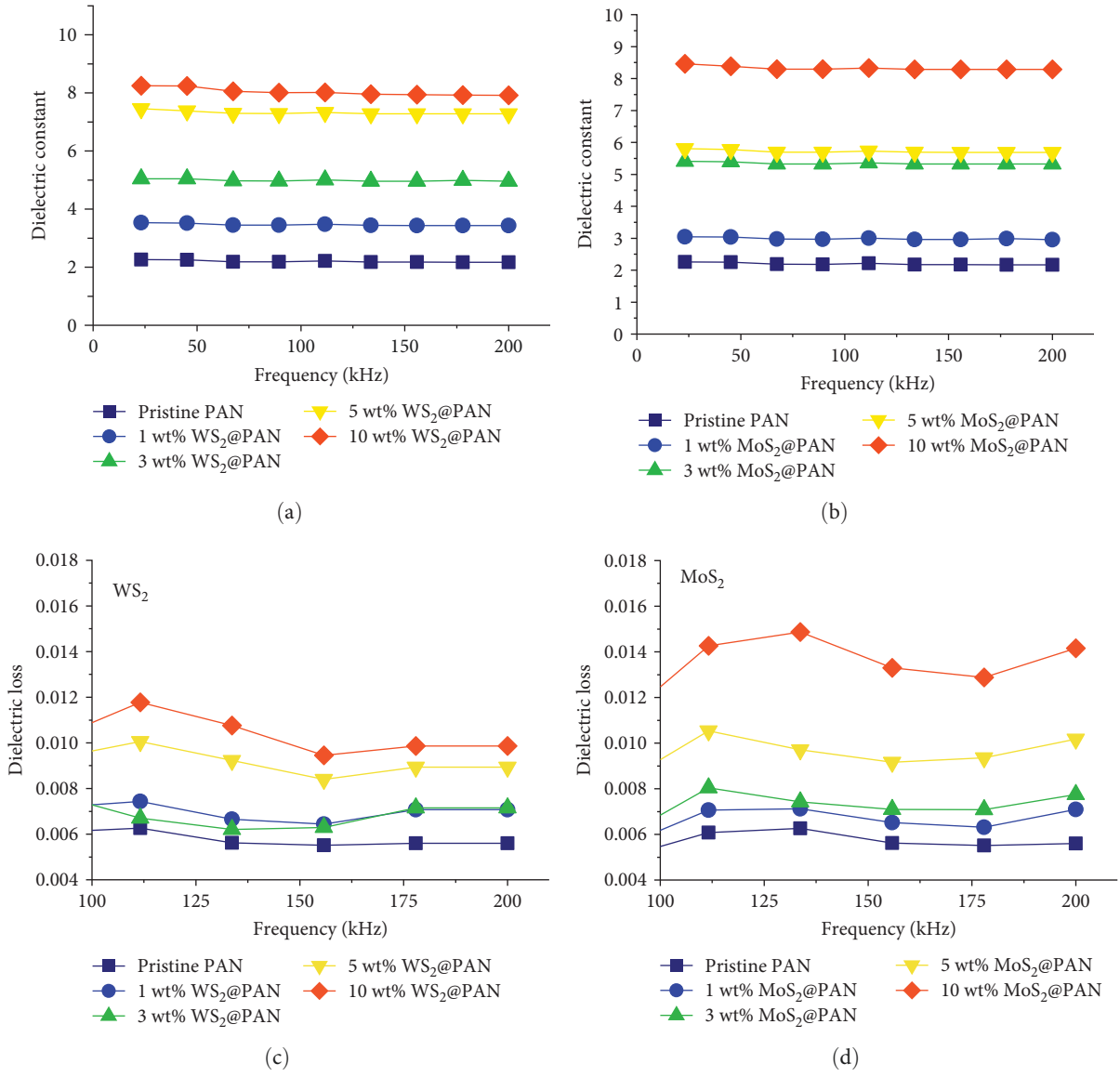

FIGURE 8: Dielectric constants of PAN nanofibers doped with (a) WS_2 and (b) MoS_2 measured at various frequencies. Dielectric losses of PAN nanofibers doped with (c) WS_2 and (d) MoS_2 measured at different frequencies.

PAN exploits the quantum confinement effect, enhancing the tribonegative characteristics [73, 124] and overall electrical performance of the TENGs. The addition of MoS_2 or WS_2 may have also contributed to the creation of regions near the surface of tribonegative PAN nanofibers that capture and entrap electrons. Their innate tendency to absorb and confine electrons enhances charge transfer and prolongs the retention of transferred charges on the friction surfaces. Consequently, when the nanocomposite acquires more electrons, the PVB material on the opposing side also donates more electrons, leading to an increase in the surface charge densities of both materials. According to Equation (8), an increase in surface charge density directly correlates with enhanced TENG electrical outputs, while heightened charge confinement helps prevent performance drop. However, it was observed that when MoS_2 or WS_2 were added in concentrations exceeding 5 wt%, the performance of the TENGs decreased. The increase in MoS_2 or WS_2 concentration may have adversely impacted the materials' contact properties due to agglomeration, which leads to clustering on the nanofibers' surfaces and potentially diminishes contact electrification. A similar effect was noted in the literature when the concentration of MoS_2 added to PVDF reached 1 wt% [90].

In Equation (8) (V–Q–x relationship) the dielectric constant is a critical material property influencing the electrical output of TENGs. Increasing the dielectric constant can significantly enhance the electrical performance of TENGs, though this is dependent on the operational conditions. Theoretical investigations using numerical solutions of Equation (14) have been crucial for understanding how various operational conditions and material properties affect TENG performance, isolating the contributions of individual parameters [105, 125, 126, 127, 128, 129]. However, in physical experiments, independently controlling and modifying these material properties without influencing

other parameters remains a significant challenge. For instance, any alteration in material composition tends to simultaneously affect its dielectric constant, triboelectric polarity, and surface roughness. According to the *V*–*Q*–*x* relationship, the role of the dielectric constant is also dependent on the load resistance. Under constant surface charge density, lowering the load resistance increases the impact of the dielectric constant. This is particularly evident in short-circuit current conditions, as shown in Equation (11), where the dielectric constant becomes increasingly influential. Conversely, the open-circuit voltage (Equation (9)) under no current conditions is unaffected by changes in the dielectric constant. This observation, supported by simulation studies, also indicates that when surface charge density and other parameters are kept constant, changes in the dielectric constant do not significantly impact the power output of TENGs [127]. However, it is important to note that the dielectric constant does influence the surface charge density. Based on capacitive behavior principles, the displacement field (*D*) concept explains the relationship between the dielectric constant and TENG performance. In a parallel plate capacitor, the triboelectric charge density (σ) equals the magnitude of *D*, formulated as follows [101]:

$$\sigma = \frac{Q}{S} = D = \varepsilon_0 \varepsilon_r E. \tag{15}$$

Here, *E* denotes the electric field strength. The surface charge density depends on the material's dielectric constant, so the open-circuit voltage also depends on this property. Moreover, the impact of the dielectric constant on contact electrification, and therefore on surface charge density, has been shown to be more significant than the effects of the materials' triboelectric polarities in certain cases [101]. Introducing nanoparticles within the material increases the dielectric constant, thereby enhancing TENG performance. However, some experimental investigations in the literature have revealed a reduction in TENG electrical performance beyond a specific concentration of these particles. While an increase in the dielectric constant was observed, particle clustering at the contact surface resulted in diminished performance [71]. Figure 8 shows the variations in dielectric constants for pristine PAN and PAN with MoS_2 or WS_2 additives at different frequencies. The incorporation of MoS_2 or WS_2 consistently increased the dielectric constant. This increase in dielectric constant led to enhanced TENG performance. However, TENG performance has been observed to decline beyond an additive rate of 5 wt%. This decline could be linked to increased dielectric losses, resulting from misaligned dipoles and energy loss due to the addition of MoS_2 or WS_2 [90, 130].

4. Conclusion

TENGs are devices that generate electric current by contact electrification and electrostatic induction. Their widespread use depends on increasing their performance. In this study, we aimed to improve the triboelectric properties of polyacrylonitrile (PAN) nanofibers by incorporating transition metal dichalcogenides, MoS_2 and WS_2, to produce high performance TENGs. Nanofibers were preferred due to their flexible structure, simple fabrication techniques, and large contact surface areas. MoS_2 and WS_2 doped nanofibers were fabricated using the electrospinning method. The surface morphology of the produced nanofibers was investigated using SEM. The analyses revealed that MoS_2 and WS_2 doped nanofibers have thinner diameters and higher specific surface area leading to an increased contact area for the triboelectric layers. The measurements of the dielectric constant indicated that the addition of dopants increased the dielectric constant of the nanofibers, potentially leading to an increase in surface charge density. Performance tests of the TENGs evaluated the electrical output of MoS_2 and WS_2 doped nanofibers under different load resistances and capacitors. Doping with 5 wt % MoS_2 or 5 wt% WS_2 significantly increased the electrical output of the TENGs, achieving the highest output voltage and energy storage capacity at these ratios. The 5 wt% WS_2@PAN & PVB and 5 wt% MoS_2@PAN & PVB TENGs generated open circuit voltage of 1,026 V and peak power outputs of 40.5 mW, respectively. The peak power density for both TENGs was found to be 25.3 W/m^2 under 4.7 MΩ load resistance. The addition of 5 wt% MoS_2 or 5 wt% WS_2 resulted in more than a twofold increase in electrical power density compared to pristine PAN.

Data Availability

The data are available upon request.

Conflicts of Interest

The authors declare that they have no conflicts of interest.

Authors' Contributions

Abdulkerim Karabiber contributed to conceptualization, methodology, validation, investigation, writing the review, and editing. Ömer Dirik contributed to investigation, writing the review, and editing. Abdulkerim Okbaz contributed to conceptualization, methodology, validation, writing the review, and editing. Adem Yar and Abdurrahman Özen contributed to methodology, writing the review, and editing. Faruk Özel contributed to methodology, validation, investigation, writing the review, and editing.

Acknowledgments

The authors gratefully acknowledge the financial support provided by The Scientific and Technological Research Council of Türkiye (TUBITAK) under project number 121M608.

References

[1] J. Li, J. Chen, and H. Guo, "Triboelectric nanogenerators for harvesting wind energy: recent advances and future perspectives," *Energies*, vol. 14, no. 21, Article ID 6949, 2021.

[2] Z. Ren, L. Wu, Y. Pang, W. Zhang, and R. Yang, "Strategies for effectively harvesting wind energy based on triboelectric nanogenerators," *Nano Energy*, vol. 100, Article ID 107522, 2022.

[3] J. Han, Y. Feng, P. Chen et al., "Wind-driven soft-contact rotary triboelectric nanogenerator based on rabbit fur with

high performance and durability for smart farming," *Advanced Functional Materials*, vol. 32, no. 2, pp. 1–8, 2022.

[4] C. Zhang, Y. Liu, B. Zhang et al., "Harvesting wind energy by a triboelectric nanogenerator for an intelligent high-speed train system," *ACS Energy Letters*, vol. 6, pp. 1490–1499, 2021.

[5] A. M. Nazar, K. J. I. Egbe, A. Abdollahi, and M. A. Hariri-Ardebili, "Triboelectric nanogenerators for energy harvesting in ocean: a review on application and hybridization," *Energies*, vol. 14, no. 18, Article ID 5600, 2021.

[6] C. Song, X. Zhu, M. Wang et al., "Recent advances in ocean energy harvesting based on triboelectric nanogenerators," *Sustainable Energy Technologies and Assessments*, vol. 53, Article ID 102767, 2022.

[7] S. Radhakrishnan, S. Joseph, E. J. Jelmy, K. J. Saji, T. Sanathanakrishnan, and H. John, "Triboelectric nanogenerators for marine energy harvesting and sensing applications," *Results in Engineering*, vol. 15, Article ID 100487, 2022.

[8] Z. Deng, L. Xu, H. Qin et al., "Rationally structured triboelectric nanogenerator arrays for harvesting water-current energy and self-powered sensing," *Advanced Materials*, vol. 34, Article ID 2205064, 2022.

[9] J. Lv, J. Chen, and P. S. Lee, "Sustainable wearable energy storage devices self-charged by human-body bioenergy," *SusMat*, vol. 1, no. 2, pp. 285–302, 2021.

[10] Y. Zou, L. Bo, and Z. Li, "Recent progress in human body energy harvesting for smart bioelectronic system," *Fundamental Research*, vol. 1, no. 3, pp. 364–382, 2021.

[11] R. Zhang, M. Hummelgård, J. Örtegren et al., "The triboelectricity of the human body," *Nano Energy*, vol. 86, Article ID 106041, 2021.

[12] Q. H. Nguyen, Q. T. H. Ta, and N. Tran, "Review on the transformation of biomechanical energy to green energy using triboelectric and piezoelectric based smart materials," *Journal of Cleaner Production*, vol. 371, Article ID 133702, 2022.

[13] A. S. Afroz, D. Romano, F. Inglese, and C. Stefanini, "Towards bio-hybrid energy harvesting in the real-world: pushing the boundaries of technologies and strategies using bio-electrochemical and bio-mechanical processes," *Applied Sciences*, vol. 11, no. 5, Article ID 2220, 2021.

[14] X. Zhao, H. Askari, and J. Chen, "Nanogenerators for smart cities in the era of 5G and internet of things," *Joule*, vol. 5, no. 6, pp. 1391–1431, 2021.

[15] J. Luo, W. Gao, and Z. L. Wang, "The triboelectric nanogenerator as an innovative technology toward intelligent sports," *Advanced Materials*, vol. 33, no. 17, pp. 1–8, 2021.

[16] X. Yang, G. Liu, Q. Guo et al., "Triboelectric sensor array for internet of things based smart traffic monitoring and management system," *Nano Energy*, vol. 92, Article ID 106757, 2022.

[17] Y. Zhou, M. Shen, X. Cui, Y. Shao, L. Li, and Y. Zhang, "Triboelectric nanogenerator based self-powered sensor for artificial intelligence," *Nano Energy*, vol. 84, Article ID 105887, 2021.

[18] P. Ma, H. Zhu, H. Lu et al., "Design of biodegradable wheat-straw based triboelectric nanogenerator as self-powered sensor for wind detection," *Nano Energy*, vol. 86, Article ID 106032, 2021.

[19] X. Lu, H. Zhang, X. Zhao et al., "Triboelectric nanogenerator based self-powered sensor with a turnable sector structure for monitoring driving behavior," *Nano Energy*, vol. 89, Article ID 106352, 2021.

[20] A. Yar, A. Karabiber, A. Ozen, F. Ozel, and S. Coskun, "Flexible nanofiber based triboelectric nanogenerators with high power conversion," *Renewable Energy*, vol. 162, pp. 1428–1437, 2020.

[21] A. Yar, "Enhanced output performance of tetraethyl orthosilicate and graphene nanoplates-decorated nanofiber-based triboelectric nanogenerators," *Colloids and Surfaces A: Physicochemical and Engineering Aspects*, vol. 631, Article ID 127670, 2021.

[22] A. Yar, "High performance of multi-layered triboelectric nanogenerators for mechanical energy harvesting," *Energy*, vol. 222, Article ID 119949, 2021.

[23] A. Ozen, F. Ozel, Z. Kınas, A. Karabiber, and S. Polat, "Spring assisted triboelectric nanogenerator based on sepiolite doped polyacrylonitrile nanofibers," *Sustainable Energy Technologies and Assessments*, vol. 47, Article ID 101492, 2021.

[24] A. Okbaz, "GnPs/PVDF decorated thermoplastic veils to boost the triboelectric nanogenerator output performance toward highly efficient energy harvesting," *Energy Conversion and Management*, vol. 270, Article ID 116204, 2022.

[25] Z. Kınas, A. Karabiber, A. Yar et al., "High-performance triboelectric nanogenerator based on carbon nanomaterials functionalized polyacrylonitrile nanofibers," *Energy*, vol. 239, Article ID 122369, 2022.

[26] A. Okbaz, A. Karabiber, A. Yar, Z. Kınas, A. Sarılmaz, and F. Ozel, "High-performance triboelectric nanogenerator with optimized Al or Ti-embedded silicone tribomaterial," *Energy Conversion and Management*, vol. 252, Article ID 115053, 2022.

[27] A. Yar, Z. Kınas, A. Karabiber, A. Ozen, A. Okbaz, and F. Ozel, "Enhanced performance of triboelectric nanogenerator based on polyamide-silver antimony sulfide nanofibers for energy harvesting," *Renewable Energy*, vol. 179, pp. 1781–1792, 2021.

[28] S. Wang, L. Lin, Y. Xie, Q. Jing, S. Niu, and Z. L. Wang, "Sliding-triboelectric nanogenerators based on in-plane charge-separation mechanism," *Nano Letters*, vol. 13, no. 5, pp. 2226–2233, 2013.

[29] S. Niu, Y. Liu, S. Wang et al., "Theoretical investigation and structural optimization of single-electrode triboelectric nanogenerators," *Advanced Functional Materials*, vol. 24, no. 22, pp. 3332–3340, 2014.

[30] S. Wang, Y. Xie, S. Niu, L. Lin, and Z. L. Wang, "Freestanding triboelectric-layer-based nanogenerators for harvesting energy from a moving object or human motion in contact and non-contact modes," *Advanced Materials*, vol. 26, no. 18, pp. 2818–2824, 2014.

[31] Z. Liu, H. Li, B. Shi, Y. Fan, Z. L. Wang, and Z. Li, "Wearable and implantable triboelectric nanogenerators," *Advanced Functional Materials*, vol. 29, no. 20, pp. 1–19, 2019.

[32] F. Yi, J. Wang, X. Wang et al., "Stretchable and waterproof self-charging power system for harvesting energy from diverse deformation and powering wearable electronics," *ACS Nano*, vol. 10, no. 7, pp. 6519–6525, 2016.

[33] H. Guo, M.-H. Yeh, Y.-C. Lai et al., "All-in-one shape-adaptive self-charging power package for wearable electronics," *ACS Nano*, vol. 10, no. 11, pp. 10580–10588, 2016.

[34] G. Zhu, P. Bai, J. Chen, and Z. L. Wang, "Power-generating shoe insole based on triboelectric nanogenerators for self-powered consumer electronics," *Nano Energy*, vol. 2, no. 5, pp. 688–692, 2013.

[35] S. Niu, X. Wang, F. Yi, Y. S. Zhou, and Z. L. Wang, "A universal self-charging system driven by random biomechanical energy for sustainable operation of mobile electronics," *Nature Communications*, vol. 6, no. 1, 2015.

[36] J. Chen, G. Zhu, W. Yang et al., "Harmonic-resonator-based triboelectric nanogenerator as a sustainable power source and a self-powered active vibration sensor," *Advanced Materials*, vol. 25, no. 42, pp. 6094–6099, 2013.

[37] X. Xiao, X. Zhang, S. Wang et al., "Honeycomb structure inspired triboelectric nanogenerator for highly effective vibration energy harvesting and self-powered engine condition monitoring," *Advanced Energy Materials*, vol. 9, no. 40, pp. 1–11, 2019.
[38] Y. Qi, G. Liu, Y. Gao et al., "Frequency band characteristics of a triboelectric nanogenerator and ultra-wide-band vibrational energy harvesting," *ACS Applied Materials & Interfaces*, vol. 13, no. 22, pp. 26084–26092, 2021.
[39] T. Quan, Y. Wu, and Y. Yang, "Hybrid electromagnetic–triboelectric nanogenerator for harvesting vibration energy," *Nano Research*, vol. 8, no. 10, pp. 3272–3280, 2015.
[40] K. Wang, J. Zhou, H. Ouyang, Y. Chang, and D. Xu, "A dual quasi-zero-stiffness sliding-mode triboelectric nanogenerator for harvesting ultralow-low frequency vibration energy," *Mechanical Systems and Signal Processing*, vol. 151, Article ID 107368, 2021.
[41] Z. Yuan, C. Wang, J. Xi et al., "Spherical triboelectric nanogenerator with dense point contacts for harvesting multidirectional water wave and vibration energy," *ACS Energy Letters*, vol. 6, no. 8, pp. 2809–2816, 2021.
[42] Y. Zhao, Z. Fan, C. Bi, H. Wang, J. Mi, and M. Xu, "On hydrodynamic and electrical characteristics of a self-powered triboelectric nanogenerator based buoy under water ripples," *Applied Energy*, vol. 308, Article ID 118323, 2022.
[43] X. Liang, Z. Liu, Y. Feng et al., "Spherical triboelectric nanogenerator based on spring-assisted swing structure for effective water wave energy harvesting," *Nano Energy*, vol. 83, Article ID 105836, 2021.
[44] W. Sun, Y. Zheng, T. Li et al., "Liquid-solid triboelectric nanogenerators array and its applications for wave energy harvesting and self-powered cathodic protection," *Energy*, vol. 217, Article ID 119388, 2021.
[45] Y. Su, X. Wen, G. Zhu et al., "Hybrid triboelectric nanogenerator for harvesting water wave energy and as a self-powered distress signal emitter," *Nano Energy*, vol. 9, pp. 186–195, 2014.
[46] S. L. Zhang, M. Xu, C. Zhang et al., "Rationally designed sea snake structure based triboelectric nanogenerators for effectively and efficiently harvesting ocean wave energy with minimized water screening effect," *Nano Energy*, vol. 48, pp. 421–429, 2018.
[47] P. Cheng, H. Guo, Z. Wen et al., "Largely enhanced triboelectric nanogenerator for efficient harvesting of water wave energy by soft contacted structure," *Nano Energy*, vol. 57, pp. 432–439, 2019.
[48] Y. Yang, G. Zhu, H. Zhang et al., "Triboelectric nanogenerator for harvesting wind energy and as self-powered wind vector sensor system," *ACS Nano*, vol. 7, no. 10, pp. 9461–9468, 2013.
[49] M.-L. Seol, J.-H. Woo, S.-B. Jeon et al., "Vertically stacked thin triboelectric nanogenerator for wind energy harvesting," *Nano Energy*, vol. 14, pp. 201–208, 2015.
[50] L. Zhang, B. Zhang, J. Chen et al., "Lawn structured triboelectric nanogenerators for scavenging sweeping wind energy on rooftops," *Advanced Materials*, vol. 28, no. 8, pp. 1650–1656, 2016.
[51] A. Ahmed, M. F. El-Kady, I. Hassan et al., "Fire-retardant, self-extinguishing triboelectric nanogenerators," *Nano Energy*, vol. 59, pp. 336–345, 2019.
[52] H. Zhang, Y. Lu, A. Ghaffarinejad, and P. Basset, "Progressive contact-separate triboelectric nanogenerator based on conductive polyurethane foam regulated with a Bennet doubler conditioning circuit," *Nano Energy*, vol. 51, pp. 10–18, 2018.
[53] X. Cui, S. Cao, Z. Yuan et al., "Electrode-free triboelectric nanogenerator for harvesting human biomechanical energy and as a versatile inartificial physiological monitor," *Energy Technology*, vol. 7, no. 5, pp. 1–7, 2019.
[54] X. Chen, L. Miao, H. Guo et al., "Waterproof and stretchable triboelectric nanogenerator for biomechanical energy harvesting and self-powered sensing," *Applied Physics Letters*, vol. 112, no. 20, pp. 1–6, 2018.
[55] P. S. Das, A. Chhetry, P. Maharjan, M. S. Rasel, and J. Y. Park, "A laser ablated graphene-based flexible self-powered pressure sensor for human gestures and finger pulse monitoring," *Nano Research*, vol. 12, no. 8, pp. 1789–1795, 2019.
[56] S. Chun, I. Y. Choi, W. Son et al., "High-output and bending-tolerant triboelectric nanogenerator based on an interlocked array of surface-functionalized indium tin oxide nanohelixes," *ACS Energy Letters*, vol. 4, no. 7, pp. 1748–1754, 2019.
[57] N. Gogurla, B. Roy, J.-Y. Park, and S. Kim, "Skin-contact actuated single-electrode protein triboelectric nanogenerator and strain sensor for biomechanical energy harvesting and motion sensing," *Nano Energy*, vol. 62, pp. 674–681, 2019.
[58] Y. Wu, Y. Luo, J. Qu, W. A. Daoud, and T. Qi, "Liquid single-electrode triboelectric nanogenerator based on graphene oxide dispersion for wearable electronics," *Nano Energy*, vol. 64, Article ID 103948, 2019.
[59] A. S. M. I. Uddin, U. Yaqoob, and G.-S. Chung, "Improving the working efficiency of a triboelectric nanogenerator by the semimetallic PEDOT: PSS hole transport layer and its application in self-powered active acetylene gas sensing," *ACS Applied Materials & Interfaces*, vol. 8, no. 44, pp. 30079–30089, 2016.
[60] X. Pu, H. Guo, Q. Tang et al., "Rotation sensing and gesture control of a robot joint via triboelectric quantization sensor," *Nano Energy*, vol. 54, pp. 453–460, 2018.
[61] X. Chen, Y. Wu, J. Shao et al., "On-skin triboelectric nanogenerator and self-powered sensor with ultrathin thickness and high stretchability," *Small*, vol. 13, no. 47, pp. 1–10, 2017.
[62] H. Chen, L. Bai, T. Li et al., "Wearable and robust triboelectric nanogenerator based on crumpled gold films," *Nano Energy*, vol. 46, pp. 73–80, 2018.
[63] Y. Zhou, W. Deng, J. Xu, and J. Chen, "Engineering materials at the nanoscale for triboelectric nanogenerators," *Cell Reports Physical Science*, vol. 1, no. 8, Article ID 100142, 2020.
[64] H. Chen, Y. Xu, L. Bai et al., "Crumpled graphene triboelectric nanogenerators: smaller devices with higher output performance," *Advanced Materials Technologies*, vol. 2, no. 6, pp. 1–7, 2017.
[65] H. Chen, Y. Xu, J. Zhang, W. Wu, and G. Song, "Enhanced stretchable graphene-based triboelectric nanogenerator via control of surface nanostructure," *Nano Energy*, vol. 58, pp. 304–311, 2019.
[66] I.-W. Tcho, W.-G. Kim, S.-B. Jeon et al., "Surface structural analysis of a friction layer for a triboelectric nanogenerator," *Nano Energy*, vol. 42, pp. 34–42, 2017.
[67] H. Wang, M. Shi, K. Zhu et al., "High performance triboelectric nanogenerators with aligned carbon nanotubes," *Nanoscale*, vol. 8, no. 43, pp. 18489–18494, 2016.

[68] G. Zhu, C. Pan, W. Guo et al., "Triboelectric-generator-driven pulse electrodeposition for micropatterning," *Nano Letters*, vol. 12, no. 9, pp. 4960–4965, 2012.

[69] J. Gong, B. Xu, and X. Tao, "Breath figure micromolding approach for regulating the microstructures of polymeric films for triboelectric nanogenerators," *ACS Applied Materials & Interfaces*, vol. 9, no. 5, pp. 4988–4997, 2017.

[70] G. Suo, Y. Yu, Z. Zhang et al., "Piezoelectric and triboelectric dual effects in mechanical-energy harvesting using $BaTiO_3$/polydimethylsiloxane composite film," *ACS Applied Materials & Interfaces*, vol. 8, no. 50, pp. 34335–34341, 2016.

[71] J. Chen, H. Guo, X. He et al., "Enhancing performance of triboelectric nanogenerator by filling high dielectric nanoparticles into sponge PDMS film," *ACS Applied Materials & Interfaces*, vol. 8, no. 1, pp. 736–744, 2016.

[72] D. Park, S.-H. Shin, I.-J. Yoon, and J. Nah, "Ferroelectric nanoparticle-embedded sponge structure triboelectric generators," *Nanotechnology*, vol. 29, no. 18, Article ID 185402, 2018.

[73] C. Wu, T. W. Kim, J. H. Park et al., "Enhanced triboelectric nanogenerators based on MoS_2 monolayer nanocomposites acting as electron-acceptor layers," *ACS Nano*, vol. 11, no. 8, pp. 8356–8363, 2017.

[74] H.-W. Park, N. D. Huynh, W. Kim et al., "Electron blocking layer-based interfacial design for highly-enhanced triboelectric nanogenerators," *Nano Energy*, vol. 50, pp. 9–15, 2018.

[75] S.-N. Chen, M.-Z. Huang, Z.-H. Lin, and C.-P. Liu, "Enhancing charge transfer for ZnO nanorods based triboelectric nanogenerators through Ga doping," *Nano Energy*, vol. 65, Article ID 104069, 2019.

[76] S.-N. Chen, C.-H. Chen, Z.-H. Lin, Y.-H. Tsao, and C.-P. Liu, "On enhancing capability of tribocharge transfer of ZnO nanorod arrays by Sb doping for anomalous output performance improvement of triboelectric nanogenerators," *Nano Energy*, vol. 45, pp. 311–318, 2018.

[77] Y. Zhang, Z. Zhou, L. Sun, Z. Liu, X. Xia, and T. H. Tao, ""Genetically engineered", biofunctional triboelectric nanogenerators using recombinant spider silk," *Advanced Materials*, vol. 30, no. 50, pp. 1–9, 2018.

[78] X. Cheng, B. Meng, X. Chen et al., "Single-step fluorocarbon plasma treatment-induced wrinkle structure for high-performance triboelectric nanogenerator," *Small*, vol. 12, no. 2, pp. 229–236, 2016.

[79] C. Park, M. Koo, G. Song et al., "Surface-conformal triboelectric nanopores via supramolecular ternary polymer assembly," *ACS Nano*, vol. 14, no. 1, pp. 755–766, 2020.

[80] A. U. Rehman, A. M. Afzal, M. W. Iqbal et al., "Highly efficient and stable layered AgZnS@WS2 nanocomposite electrode as superior charge transfer and active redox sites for energy harvesting device," *Journal of Energy Storage*, vol. 71, Article ID 108022, 2023.

[81] J. Hu, "Review of applications and research of 2D TMDCs (WS_2 & MoS_2)," 2022, https://openscholarship.wustl.edu/mems500https://openscholarship.wustl.edu/mems500/191.

[82] M. Ali, A. M. Afzal, M. W. Iqbal et al., "2D-TMDs based electrode material for supercapacitor applications," *International Journal of Energy Research*, vol. 46, no. 15, pp. 22336–22364, 2022.

[83] M. Kim, D. Park, M. M. Alam, S. Lee, P. Park, and J. Nah, "Remarkable output power density enhancement of triboelectric nanogenerators via polarized ferroelectric polymers and bulk MoS_2 composites," *ACS Nano*, vol. 13, no. 4, pp. 4640–4646, 2019.

[84] S. Park, J. Park, Y.-G. Kim et al., "Laser-directed synthesis of strain-induced crumpled MoS_2 structure for enhanced triboelectrification toward haptic sensors," *Nano Energy*, vol. 78, Article ID 105266, 2020.

[85] S. Karmakar, R. Sarkar, C. S. Tiwary, and P. Kumbhakar, "Synthesis of bilayer MoS_2 nanosheets by green chemistry approach and its application in triboelectric and catalytic energy harvesting," *Journal of Alloys and Compounds*, vol. 844, Article ID 155690, 2020.

[86] C. Gallardo-Vega, O. López-Lagunes, O. I. Nava-Galindo et al., "Triboelectric energy harvester based on stainless steel/MoS_2 and PET/ITO/PDMS for potential smart healthcare devices," *Nanomaterials*, vol. 11, no. 6, Article ID 1533, 2021.

[87] K. Shrestha, S. Sharma, G. B. Pradhan et al., "A siloxene ecoflex nanocomposite-based triboelectric nanogenerator with enhanced charge retention by MoS_2/LIG for self-powered touchless sensor applications," *Advanced Functional Materials*, vol. 32, no. 27, Article ID 2113005, 2022.

[88] K. Zhao, W. Sun, X. Zhang et al., "High-performance and long-cycle life of triboelectric nanogenerator using PVC/MoS_2 composite membranes for wind energy scavenging application," *Nano Energy*, vol. 91, Article ID 106649, 2022.

[89] M. Kim, S. H. Kim, M. U. Park et al., "MoS_2 triboelectric nanogenerators based on depletion layers," *Nano Energy*, vol. 65, Article ID 104079, 2019.

[90] B. Hedau, B.-C. Kang, and T.-J. Ha, "Enhanced triboelectric effects of self-poled MoS_2-embedded PVDF hybrid nanocomposite films for bar-printed wearable triboelectric nanogenerators," *ACS Nano*, vol. 16, no. 11, pp. 18355–18365, 2022.

[91] T. I. Kim, I.-J. Park, S. Kang, T.-S. Kim, and S.-Y. Choi, "Enhanced triboelectric nanogenerator based on tungsten disulfide via thiolated ligand conjugation," *ACS Applied Materials & Interfaces*, vol. 13, no. 18, pp. 21299–21309, 2021.

[92] T. Chekke, R. Narzary, S. Ngadong, B. Satpati, S. Bayan, and U. Das, "Au decorated ultrathin WS_2-based single-electrode triboelectric nanogenerator for flexible self-powered photodetector," *Sensors and Actuators A: Physical*, vol. 349, Article ID 114076, 2023.

[93] T. Chekke, R. Narzary, S. Ngadong, B. Satpati, S. Bayan, and U. Das, "2D WS_2-based single-electrode triboelectric nanogenerator for power generation and motion sensing," *Journal of Electronic Materials*, vol. 52, no. 4, pp. 2685–2694, 2023.

[94] T. Chekke, R. Narzary, S. Ngadong, B. Satpati, S. Bayan, and U. Das, "Cotton based self-powered temperature sensor based on Au-augmented WS_2 triboelectric nanogenerator," *Journal of Electronic Materials*, vol. 53, no. 1, pp. 238–249, 2024.

[95] D. Semnani, "7—Geometrical characterization of electrospun nanofibers," in *Electrospun Nanofibers*, pp. 151–180, Woodhead Publishing, 2017.

[96] G. B. Medeiros, F. de A. Lima, D. S. de Almeida, V. G. Guerra, and M. L. Aguiar, "Modification and functionalization of fibers formed by electrospinning: a review," *Membranes*, vol. 12, no. 9, Article ID 861, 2022.

[97] A. Babu, I. Aazem, R. Walden, S. Bairagi, D. M. Mulvihill, and S. C. Pillai, "Electrospun nanofiber based TENGs for wearable electronics and self-powered sensing," *Chemical Engineering Journal*, vol. 452, Article ID 139060, 2023.

[98] X. Ge, N. Hu, F. Yan, and Y. Wang, "Development and applications of electrospun nanofiber-based triboelectric nanogenerators," *Nano Energy*, vol. 112, Article ID 108444, 2023.
[99] J. Yin, J. Li, S. Ramakrishna, and L. Xu, "Hybrid-structured electrospun nanofiber membranes as triboelectric nanogenerators for self-powered wearable electronics," *ACS Sustainable Chemistry & Engineering*, vol. 11, no. 38, pp. 14020–14030, 2023.
[100] J. Yin, V. S. Reddy, A. Chinnappan, S. Ramakrishna, and L. Xu, "Electrospun micro/nanofiber with various structures and functions for wearable physical sensors," *Polymer Reviews*, vol. 63, no. 3, pp. 715–762, 2023.
[101] Y. J. Kim, J. Lee, S. Park, C. Park, C. Park, and H.-J. Choi, "Effect of the relative permittivity of oxides on the performance of triboelectric nanogenerators," *RSC Advances*, vol. 7, no. 78, pp. 49368–49373, 2017.
[102] Z. L. Wang, "Triboelectric nanogenerators as new energy technology for self-powered systems and as active mechanical and chemical sensors," *ACS Nano*, vol. 7, no. 11, pp. 9533–9557, 2013.
[103] C. Zhang, W. Tang, C. Han, F. Fan, and Z. L. Wang, "Theoretical comparison, equivalent transformation, and conjunction operations of electromagnetic induction generator and triboelectric nanogenerator for harvesting mechanical energy, Adv," *Advanced Materials*, vol. 26, no. 22, pp. 3580–3591, 2014.
[104] C. Rodrigues, D. Nunes, D. Clemente et al., "Emerging triboelectric nanogenerators for ocean wave energy harvesting: state of the art and future perspectives," *Energy & Environmental Science*, vol. 13, no. 9, pp. 2657–2683, 2020.
[105] S. Niu, S. Wang, L. Lin et al., "Theoretical study of contact-mode triboelectric nanogenerators as an effective power source," *Energy & Environmental Science*, vol. 6, no. 12, pp. 3576–3583, 2013.
[106] G. Zhu, Z.-H. Lin, Q. Jing et al., "Toward large-scale energy harvesting by a nanoparticle-enhanced triboelectric nanogenerator," *Nano Letters*, vol. 13, no. 2, pp. 847–853, 2013.
[107] Z. L. Wang and A. C. Wang, "On the origin of contact-electrification," *Materials Today*, vol. 30, pp. 34–51, 2019.
[108] C. Xu, Y. Zi, A. C. Wang et al., "On the electron-transfer mechanism in the contact-electrification effect," *Advanced Materials*, vol. 30, no. 15, pp. 1–9, 2018.
[109] L. Zhao, Q. Zheng, H. Ouyang et al., "A size-unlimited surface microstructure modification method for achieving high performance triboelectric nanogenerator," *Nano Energy*, vol. 28, pp. 172–178, 2016.
[110] D. Kim, I.-W. Tcho, I. K. Jin et al., "Direct-laser-patterned friction layer for the output enhancement of a triboelectric nanogenerator," *Nano Energy*, vol. 35, pp. 379–386, 2017.
[111] J. Huang, X. Fu, G. Liu et al., "Micro/nano-structures-enhanced triboelectric nanogenerators by femtosecond laser direct writing," *Nano Energy*, vol. 62, pp. 638–644, 2019.
[112] I. W. Park, J. Choi, K. Y. Kim et al., "Vertically aligned cyclophenylalanine peptide nanowire-based high-performance triboelectric energy generator," *Nano Energy*, vol. 57, pp. 737–745, 2019.
[113] X.-W. Zhang, G.-Z. Li, G.-G. Wang et al., "High-performance triboelectric nanogenerator with double-surface shape-complementary microstructures prepared by using simple sandpaper templates," *ACS Sustainable Chemistry & Engineering*, vol. 6, no. 2, pp. 2283–2291, 2018.
[114] Y.-S. Han, S.-H. Lee, K. H. Choi, and I. Park, "Preparation and characterization of chitosan–clay nanocomposites with antimicrobial activity," *Journal of Physics and Chemistry of Solids*, vol. 71, no. 4, pp. 464–467, 2010.
[115] J. Song, L. Gao, X. Tao, and L. Li, "Ultra-flexible and large-area textile-based triboelectric nanogenerators with a sandpaper-induced surface microstructure," *Materials*, vol. 11, no. 11, Article ID 2120, 2018.
[116] M. Seol, S. Kim, Y. Cho et al., "Triboelectric series of 2D layered materials," *Advanced Materials*, vol. 30, no. 39, 2018.
[117] M. Baalousha, W. How, E. Valsami-Jones, and J. R. Lead, "Chapter 1—overview of environmental nanoscience," *Frontiers of Nanoscience*, vol. 7, pp. 1–54, 2014.
[118] C. Ma, H. Zhu, J. Zhou et al., "Confinement effect of monolayer MoS_2 quantum dots on conjugated polyimide and promotion of solar-driven photocatalytic hydrogen generation," *Dalton Transactions*, vol. 46, no. 12, pp. 3877–3886, 2017.
[119] G. H. Shin, C.-K. Kim, G. S. Bang et al., "Multilevel resistive switching nonvolatile memory based on MoS_2 nanosheet-embedded graphene oxide," *2D Materials*, vol. 3, no. 3, Article ID 034002, 2016.
[120] J. Liu, Z. Zeng, X. Cao et al., "Preparation of MoS_2-polyvinylpyrrolidone nanocomposites for flexible nonvolatile rewritable memory devices with reduced graphene oxide electrodes," *Small*, vol. 8, no. 22, pp. 3517–3522, 2012.
[121] S. Das, M. Dandu, G. Gupta et al., "Highly tunable layered exciton in bilayer WS_2: linear quantum confined stark effect versus electrostatic doping," *ACS Photonics*, vol. 7, no. 12, pp. 3386–3393, 2020.
[122] S.-W. Zheng, L. Wang, H.-Y. Wang, C.-Y. Xu, Y. Luo, and H.-B. Sun, "Observation of quantum-confined exciton states in monolayer WS_2 quantum dots by ultrafast spectroscopy," *Nanoscale*, vol. 13, no. 40, pp. 17093–17100, 2021.
[123] C. S. Lau, J. Y. Chee, L. Cao et al., "Gate-defined quantum confinement in CVD 2D WS_2," *Advanced Materials*, vol. 34, no. 25, 2022.
[124] M. Sharma, P. Jamdagni, A. Kumar, and P. K. Ahluwalia, "Electronic and dielectric properties of MoS2-MoX2 heterostructures," *AIP Conference Proceedings*, vol. 1661, Article ID 080028, 2015.
[125] S. Niu, Y. Liu, Y. S. Zhou, S. Wang, L. Lin, and Z. L. Wang, "Optimization of triboelectric nanogenerator charging systems for efficient energy harvesting and storage," *IEEE Transactions on Electron Devices*, vol. 62, no. 2, pp. 641–647, 2015.
[126] C. Jiang, K. Dai, F. Yi, Y. Han, X. Wang, and Z. You, "Optimization of triboelectric nanogenerator load characteristics considering the air breakdown effect," *Nano Energy*, vol. 53, pp. 706–715, 2018.
[127] H. Chen, Y. Xu, J. Zhang, W. Wu, and G. Song, "Theoretical system of contact-mode triboelectric nanogenerators for high energy conversion efficiency," *Nanoscale Research Letters*, vol. 13, no. 1, 2018.
[128] S. Niu, Y. S. Zhou, S. Wang et al., "Simulation method for optimizing the performance of an integrated triboelectric nanogenerator energy harvesting system," *Nano Energy*, vol. 8, pp. 150–156, 2014.
[129] A. Yar, A. Okbaz, and S.Ş. Parlayıcı, "A biocompatible, eco-friendly, and high-performance triboelectric nanogenerator based on sepiolite, bentonite, and kaolin decorated chitosan composite film," *Nano Energy*, vol. 110, Article ID 108354, 2023.
[130] A. M. Chandran and P. K. S. Mural, "Surface silanized MWCNTs doped PVDF nanocomposite with self-organized dipoles: an intrinsic study on the dielectric, piezoelectric, ferroelectric, and energy harvesting phenomenology," *Sustainable Energy & Fuels*, vol. 6, no. 6, pp. 1641–1653, 2022.